Predicting targeted- and immunotherapeutic response outcomes in melanoma with single-cell Raman Spectroscopy and AI

Kai Chang[1]*, Mamatha Serasanambati[2], Baba Ogunlade[3], Hsiu-Ju Hsu[2], James Agolia[2], Ariel Stiber[3], Jeffrey Gu[4], Saurabh Sharma[2], Jay Chadokiya[2], Amanda Gonçalves[2], Fareeha Safir[5], Nhat Vu[5], Daniel Delitto[2], Amanda Kirane[2*#], and Jennifer Dionne[3,6,7*#]

[1]Department of Electrical Engineering, Stanford University
350 Jane Stanford Way, Stanford, CA 94305, USA

[2]Department of Surgery, Stanford University
1201 Welch Road, MSLS, Palo Alto, CA 94304, USA

[3]Department of Materials Science and Engineering, Stanford University
496 Lomita Mall, Stanford, CA 94305, USA

[4]Department of Computational and Mathematical Engineering, Stanford University
475 Via Ortega, Stanford, CA 94305, USA

[5]Pumpkinseed Technologies, Inc.
Palo Alto, California 94306, United States

[6]Department of Radiology, Stanford University
300 Pasteur Drive Stanford, CA 94305, USA

[7]Chan Zuckerberg Biohub
499 Illinois St, San Francisco, CA 94158, USA

*to whom correspondence should be addressed: kaichang@stanford.edu, akirane@stanford.edu, jdionne@stanford.edu
#denotes equal contribution

Abstract

Identifying predictive biomarkers of immunotherapeutic response in melanoma remains an outstanding challenge. Existing transcriptomic and proteomic profiling methods of the tumor-immune microenvironment are costly and may not faithfully capture modifications actively impacting tumor behavior. Here, we present a non-destructive, single-cell approach combining Raman spectroscopy and machine learning (ML) that enables rapid cell profiling and therapeutic response prediction. We tested mouse and human melanoma cell lines alongside nine melanoma patient-derived samples. Each sample had known resistance profiles to a panel of targeted and immunotherapeutic inhibitors, including bemcentinib, cabozantinib, dabrafenib, nivolumab, and a combination of nivolumab and relatlimab. In cell lines, our single-cell Raman and ML approach achieved >96% differentiation accuracy across tumor microenvironment cell types and functional phenotypes. Formations of subclusters for persistent (e.g. drug-resistant) cells were observed based on genetic mutations rather than sample origin, with Raman signatures reflecting biochemical changes relevant to various therapeutic pathways. For patient samples, we constructed a two-stage evaluation workflow to assess clinical drug resistance. Using therapy-specific random forests, our workflow correctly inferred resistance likelihoods for 30 of 33 clinically relevant patient-drug combinations (91% accuracy) unseen by our model with optimized labeling thresholds. Our scalable, prognostic model using single-cell Raman offers potential to advance clinical, multi-omic biomarker efforts and impact first- and second-line therapy selection assessments for precision medicine.

Introduction

Precision oncology has revolutionized the standard of care for melanoma patients, improving survival rates and demonstrating durable cancer control. Systemic therapies using targeted inhibitors and immunotherapeutic agents have palliated symptoms and prolonged survival for patients with malignant and metastatic neoplasms. Immunotherapies are the standard first-line treatments for metastatic melanoma, yet demonstrate an overall response rate of <40-50% and carry a 30-50% risk of severe adverse events[1–3]. With melanoma's genomic instability and intratumoral heterogeneity in the tumor immune microenvironment (TIME), faithful profiling of biomarkers correlating to therapeutic response remains limited and represents a critical juncture towards improving patient outcomes[4–7].

Current single-cell transcriptomic and proteomic methods, although highly detailed, may not always capture the structural or post-translational modifications of biomarkers actively impacting response[4,8,9]. These approaches also require destructive or invasive protocols such as cell lysis and antibody tagging and are costly and time-intensive. Even in combination with nominally invasive immunoassays, they are poorly predictive with limited adoption as routine point-of-care tools. As such, high-throughput, high-resolution, and ideally non-destructive methods that adaptively forecast patient therapeutic response by observing the complete cellular makeup remain desirable.

Raman spectroscopy has garnered attention as a viable single-cell profiling tool that is both non-destructive and label-free. Spontaneous Raman scattering is the inelastic scattering of

photons from the molecular vibrations of a sample. These scattered photons result in a spectrum rich in biochemical information, known as the molecular fingerprint, that provides interpretable insights into the molecular structure, composition, and function of the target. In cells, the captured vibrational spectra provide information-dense profiles comprising nucleic acids, proteins, metabolites, and lipids. Recently, Raman spectroscopy has shown promise as a rapid, high-throughput tool for single-cell phenotyping, from classifying cells at an organ level to identifying subtypes in breast cancer[10,11]. This technique has also been extended to classify drug resistance in bacteria and cancer cell lines, for example accurately screening antibiotic susceptibility in tuberculosis samples and assessing vemurafenib resistance in melanoma cell lines[12,13]. Continued development of Raman as a multi-omic approach for monitoring the response of multicellular ecosystems to precision therapy presents a major opportunity in biology and medicine.

In this work, we demonstrate that single-cell Raman spectroscopy with machine learning can 1) discriminate among cell phenotypes, 2) identify biomarkers relevant to environmental responses, and 3) determine resistance to targeted therapy and immunotherapy in clinically relevant melanoma samples. We first demonstrate our capacity to identify different cancer and immune cells commonly found in the TIME, including their functional states. We then track biochemical changes in murine and human cell lines associated with treatment outcomes. We find that spectral changes shared among persistent cells coincide with potential resistance mechanisms corresponding to targeted pathways of AXL inhibitor bemcentinib[14–16], multiple tyrosine kinases inhibitor cabozantinib[17–19], BRAF inhibitor dabrafenib[20], PD-1 immune checkpoint inhibitor (ICI) nivolumab[21], and the combination immunotherapy of nivolumab with LAG-3 inhibitor relatlimab[22]. Finally, we leverage patient-derived tumor lines to construct a classification model capable of determining resistance to precision therapies. With a limited patient set, our approach correctly identifies 26 of 33 patient-drug responses, and using optimized cutoffs for each therapy further improves our assessment to 30 of 33 outcomes. Our findings show Raman could serve as a powerful phenotyping tool to bridge critical gaps in multi-omics research and omics integration into the clinical space.

Results

Tumor immune microenvironment cell differentiation

Monolayers of fixed TIME-relevant cells including cancer cells, immune cells, and patient-derived tumor cell cultures were deposited on gold-coated glass slides (Figure 1a). Across heterogeneous sets of cells that were responsive and nonresponsive to therapy, we examined Raman spectra across the biological fingerprint region from 600 to 1800 cm^{-1} (Figure 1b). We constructed reference datasets of >47,000 spectra from cancer cells and immune cell lines and augmented our dataset with an additional >27,000 spectra from clinical melanoma patient samples. Spectral barcodes were constructed from averaged differential intensities to identify biochemical bands indicative of treatment response (Figure 1b). Two-dimensional Uniform Manifold Approximation and Projection (UMAP) visualization was used to reveal biochemical variations across samples (Figure 1c). For our resistance determination architecture, a patient-resistance training matrix was constructed using human cell lines and patients with known clinical (outcome) or *in vitro* therapeutic response (cell viability) (Figure 1d,

Supplementary Table 1). After feature reduction via principal component analysis (PCA), random forests (RF) were trained for cell phenotype classification and drug resistance prognosis. Patient resistance determination was heuristically assessed through aggregated labeling, where the likelihood was calculated by the resistance distribution of subsets of spectra (see Methods).

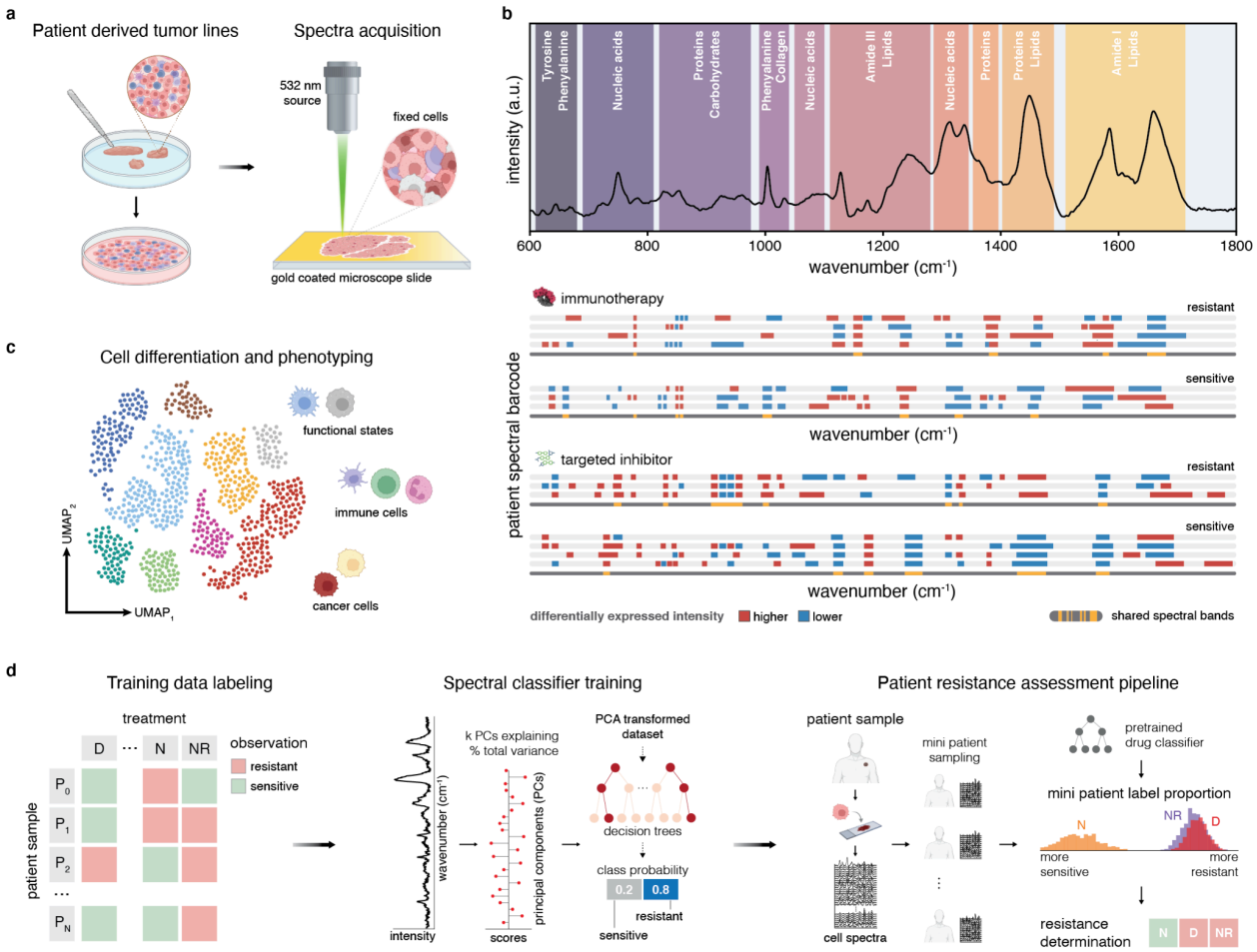

Figure 1. Overview of Raman-based profiling architecture. A) Spectral acquisition overview. Cells from commercial cell lines and patient-derived cell lines were cultured and fixed prior to drop casting onto a gold-coated microscope slide. Spectra are acquired by confocal Raman imaging at a 532 nm excitation wavelength at few- to single-cell resolution. B) Biological Raman window, also known as the optical fingerprint regime, of a cell. Averaged spectra of RAW264.7 macrophages, with major band assignments highlighting cellular makeup. Differential Raman "expression" profiles or spectral barcodes generated from cell spectra are used to delineate samples and drug response. C) UMAP embeddings of melanoma spectra are analyzed by nonlinear dimensionality reduction to examine cell states and phenotypes. D) Patient-derived cell lines resistance determination workflow. Patient clinical response and in-vitro treatment response outcomes are used to label spectral data. Patient-derived cell spectra are collected and reduced using PCA, and a random forest is trained to determine resistance likelihood per spectrum. For an unseen patient, groupings of finite sets of spectra (mini patients) are generated by sampling the patient spectral set. Mini patient label distributions, determined by our pre-trained single spectrum classifier, are used to determine patient resistance to targeted inhibitors and immunotherapies.

We first assessed cell type and phenotype differentiability by selecting commercial murine melanoma and immune cell lines that span relevant conditions residing in the TIME: distinct cell types (macrophage RAW264.7 and cancer cells), low and high somatic mutations (melanoma YUMM1.7 and YUMMER1.7), and intertumoral heterogeneity (melanoma B16-F10 and LN6-Engleman)[23–25].

We collected an average (μ_{cells}) of 1000+ few-to-single-cell spectra per cell line. SEM images of our samples confirmed relative monocell density and uniformity across acquisition regions (Figure 2a). Mean Raman spectra (Figure 2b) of these murine melanoma and immune cell lines are visually distinguishable based on their vibrational peaks. Notably, peak intensities vary across wavenumbers corresponding to phenylalanine (1003, 1606), nucleic acids (667, 748, 780, 1306, 1337, 1585), proteins (748, 1126, 1336, 1446, 1585, 1664), and lipids (1306, 1446 cm^{-1})[10,26–29]; complete biological peak assignments are in Supplementary Table 4. UMAP performed on the top 50 principal components, which accounted for >95% of the spectral variance, shows neighboring YUMM1.7 and B16-F10 groupings (Figure 2b) attributed to the higher melanin presence, which was visible in optical micrographs (Supplementary Figure 1) and by Raman (1385, 1580 cm^{-1})[30,31]. We also repeated measurements across two or three days to examine environmental fluctuation effects on spectral profiles and observed minimal spectral and UMAP embedding differences (Supplementary Figure 2). We implemented an RF multiclass classifier on the PCA-reduced spectra to determine the discriminatory power of Raman. Our RF achieved an overall 96% classification accuracy in discriminating these cell lines, with >91% accuracy distinguishing between parent and derivative lines (Figure 2b).

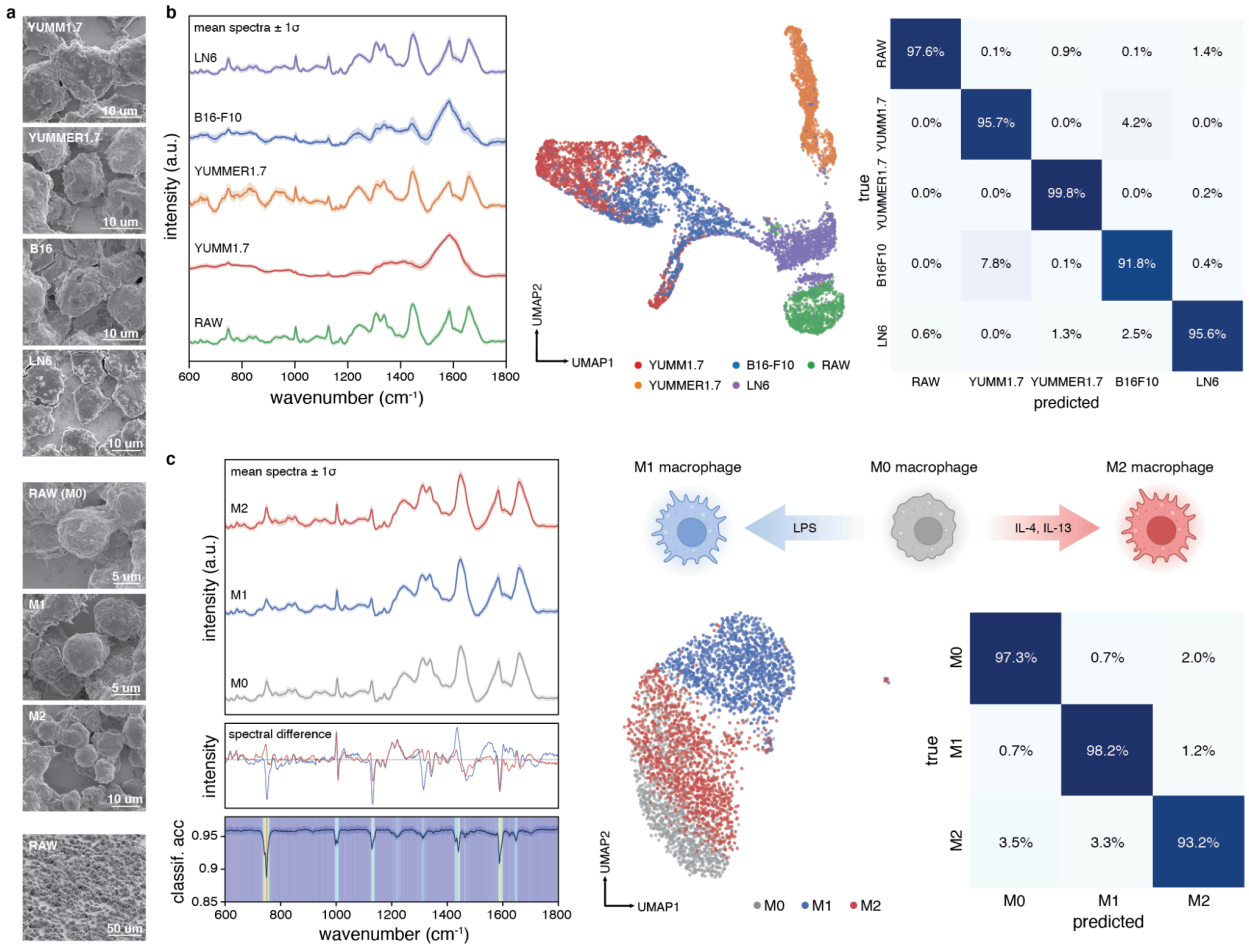

Figure 2. TIME cell type and macrophage polarization state differentiation. A) SEM micrographs of mouse melanoma (YUMM1.7, YUMMER1.7, B16-F10, LN6-Engleman) and macrophage (RAW264.7) cells highlighting minimal morphology differences. The tilted SEM micrograph (bottom) shows cellular aggregation after drying. B) Left: Mean normalized Raman spectra in the biological fingerprint regime of different melanoma and immune cells with ±1 standard deviation. Over 1000 spectra were collected for each cell type. Center: UMAP embedding of PCA-reduced Raman signal. Right: Confusion matrix generated via random forest classification, showing an average of ≥95% accuracy across cell types. C) Left: Mean normalized Raman spectra of RAW264.7 macrophages in different polarization states (M0, M1-like, M2-like) with ±1 standard deviation, spectral differences of polarization states relative to M0 (grey), and wavenumber importance as a function of dropoff in classification accuracy across states. Center: UMAP embedding of macrophage profiles. Right: Confusion matrix showing an average of ≥94% accuracy across polarizations.

Macrophage phenotype polarization

To assess whether our method could identify changes to cell activation and functional phenotypes, we analyzed Raman differences across macrophage polarization states. We exposed inert RAW264.7 macrophages (M0 labeled) to elevated concentrations of cytokines (IL-4 and IL-13) and lipopolysaccharides (LPS) for 24 hours (Figure 2c). Brightfield imaging revealed distinct morphological changes in inert M0 (circular), tumor-suppressing M1-like (spindle-like, elongated), and tumor and angiogenesis-assisting M2-like (mixed) plasticities (Supplementary Figure 1), concurrent with prior findings[32].

Physical differences greatly diminished after fixation and drop casting; SEM micrographs (Figure 2a) showed physical morphology homogeneity across dried and fixed samples. Despite physical similarities, Raman spectra (μ_{cells} = 1198) revealed differences across nucleic acids (749, 782, 1337), lipids (1310, 1655), and proteins (749, 1003, 1127, 1207, 1447, 1585, 1660 cm^{-1}) (Figure 2c)[33–36]. In low-dimensional embeddings, M1-like macrophages were distinct from M0 and M2-like macrophages, and RF classification yielded a >96% accuracy in determining macrophage polarization state. We identified 750 cm^{-1} (tryptophan) as the most significant discriminator (>7% dropoff), followed by protein and lipid bands at 1588, 1440, 1129, and 998 cm^{-1} through wavenumber importance analysis derived from classification accuracy dropoffs by spectral perturbation (Figure 2c). This suggested increased tryptophan metabolic activity, which is positively correlated with M1-like polarization[37].

Melanoma response to therapies in murine and human samples

To determine Raman sensitivity to molecular changes impacting therapeutic resistance, we investigated Raman spectra of murine and human cells pre- and post-treatment with targeted and immune checkpoint inhibitors disrupting critical metastatic melanoma progression pathways. We treated cells to IC_{50} concentrations of single-dose monotherapies bemcentinib, cabozantinib, dabrafenib, and nivolumab for 24 hours with no medium replacement (Figure 3a), and isolated surviving cells for Raman.

In our mouse model, YUMM1.7 and YUMMER1.7 spectra (μ_{cells} = 994, min: 838, max: 1146) divergence (Figure 3b) and UMAP embeddings (Figure 3d) agreed with expected responses. Post-drug exposure, YUMMER1.7 displayed more pronounced differences in Raman spectra among treatment groups, likely due to elevated, UVB-driven somatic mutations, whereas the more resistant, wild-type YUMM1.7 showed fewer post-treatment differences[23,24,38], which may be obscured by prominent melanin-related features (Supplementary Figure 1).

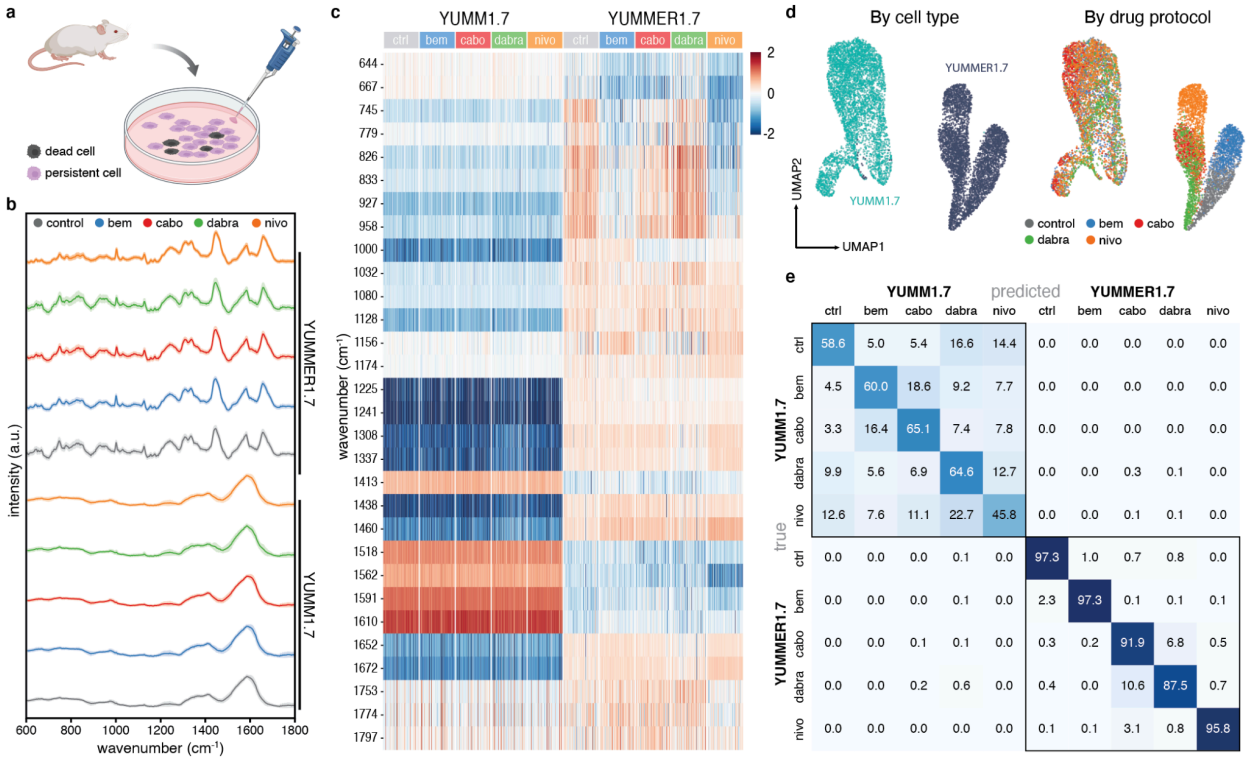

Figure 3. Targeted inhibitor and immunotherapeutic response analysis in murine melanoma cells. A) Drug treatment protocol for commercial murine melanoma cell lines. Cell viability was evaluated for each drug-treated sample, and persistent cells were isolated for Raman spectroscopy. B) Mean normalized Raman spectra and corresponding ±1 standard deviation across YUMM1.7 and YUMMER1.7 cells after exposure to various therapeutic molecules. Over 900 spectra were collected for each sample on average. C) Heatmap of major differential wavenumber bands crucial for cell discrimination, quantified by the median log2 fold change. Wavenumbers are selected from those exhibiting the most significant effect on classification accuracy. Differential Raman intensities are initially stratified by cell type of origin and further by drug protocol. D) UMAP embedding of PCA-reduced spectra from YUMM1.7 and YUMMER1.7 cell response. Left: UMAP grouped by cell type labels. Right: UMAP grouped by drug protocol (color coded grey for untreated, blue for bemcentinib (bem), red for cabozantinib (cabo), green for dabrafenib (dabra), and orange for nivolumab (nivo). E) Confusion matrix for cell type and drug treatment demonstrating higher and lower spectral discernibility for YUMMER1.7 and YUMM1.7, respectively.

Adapting scRNAseq analysis methodologies[39], we quantitatively assessed spectral disparities across the cell type-drug matrix by differential Raman "expression" (intensity) analysis, in which intensity fold changes were calculated relative to the untreated cells (Figure 3c). As expected, minimal changes were observed for YUMM, whereas distinct changes were observed for each YUMMER-drug protocol. Post-bemcentinib persistent cells showed intensity changes at 644, 667-833, 1438, 1460, and 1610 cm^{-1}, relating to tyrosine presence and phosphorylation[40–42], and elevated intensities at 1156 cm^{-1} suggested increased carotenoids and protein activity. Similar changes were observed with cabozantinib, along with a decrease at 1000 cm^{-1}. Persistent YUMMER cells post-dabrafenib showed changes at 745-958, 1000, 1032, and 1337 cm^{-1}, in alignment with their sensitivity to BRAF inhibitors[43,44]. Of note, no observed major peaks corresponded to those of relevant inhibitors (Supplementary Figure 3). For nivolumab, persistent YUMMER cell spectra were markedly different from untreated YUMMER cell spectra.

Changes in protein-affiliated peaks 745, 826, 927, 1460, 1562, and 1672 cm^{-1} and nucleic acids peaks 745, 779, and 833 cm^{-1} may be consistent with the presence of PD-1 variants (iPD-1) unique to YUMMER, resulting in cell cytostasis[45,46]. Our RF achieved a >99.1% isolate-level accuracy across and 76.4% within cell types (Figure 3e), with YUMMER presenting clearer disparities than YUMM. Detailed cell-drug one-versus-all groupings can be found in Supplementary Figure 4.

Next, we investigated single-cell Raman spectra (μ_{cells} = 1357, min: 336, max: 3327) from human commercial melanoma cell lines (A375, SK-MEL-24, and SK-MEL-30) and patient-derived tumor lines (PAT-52 and PAT-73). While untreated samples showed broadly different spectral signatures (Figure 4a-c), persistent cells of similar drug protocols formed distinct subclusters based on relevant genetic mutations rather than sample origin, displaying remarkable affinities in intensity changes (Figure 4a,c, Extended Data Figure 1).

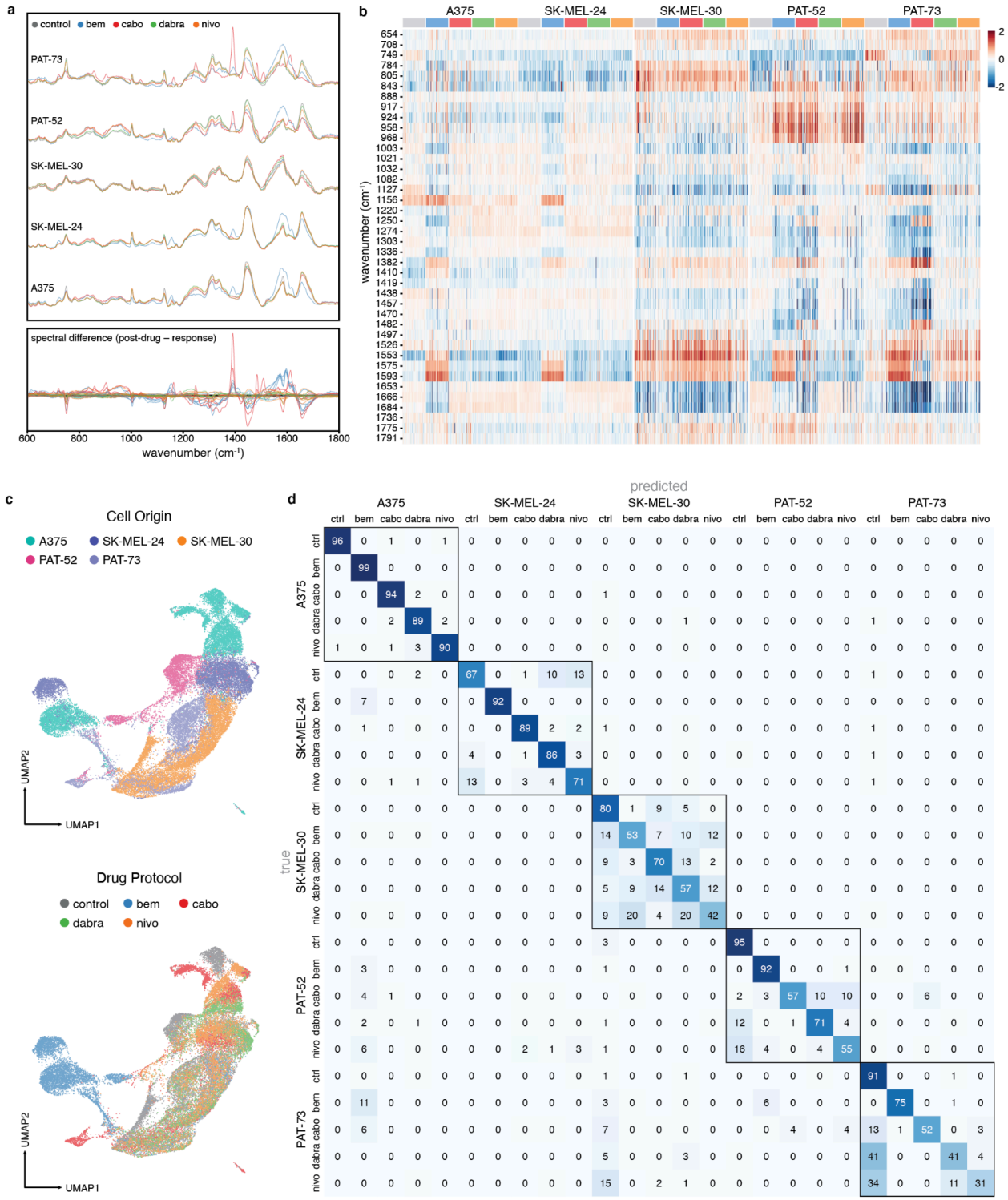

Figure 4. Targeted inhibitor and immunotherapeutic response analysis in human melanoma cell lines and patient-derived cell lines. A) Top: Mean normalized Raman spectra of cell response to treatment protocols, grouped and overlaid by patient-derived cell lines. Bottom: Spectral differences of post-treated sample relative to untreated (control), highlighting the major bands shared by similar treatment protocols across samples. B) Heatmap of differential wavenumber bands expressed in surviving cells, quantified by the median log2 fold change. C) UMAP

embedding of Raman profiles from human cell responses. Top and bottom spaces are grouped by cell type labels and drug protocol, respectively. D) Confusion matrix across cell type and drug treatment classification, demonstrating higher inter-sample differentiation and varied treatment discrimination intra-sample.

For example, AXL+ samples (A375, SK-MEL-24) showed post-bemcentinib intensity shifts clearly distinguishable by fold change (Figure 4b). Decreases in protein (1000, 1250, 1336, 1438, 1660 cm^{-1}) and lipid (1081, 1438, 1660 cm^{-1}) bands likely corresponded to tyrosine activity and AXL pathway modifications. Further, these cell spectra formed unified groupings in latent space, whereas persistent AXL- cell lines (SK-MEL-30) were indiscernible from their control (Figure 4c). Similarly, post-dabrafenib cells of wild-type BRAF samples (SK-MEL-24, SK-MEL-30) exhibited little change, whereas BRAF-positive cells (A375) showed decreases at 749, 1127, and 1526 cm^{-1}, in addition to the 1156 and 1582 cm^{-1} changes observed by Qiu et al. in A375 response to the BRAF inhibitor vemurafenib[13]. Post-cabozantinib persistent cells showed changes across protein and lipid bands with decreases at 749 and 1653-1684 cm^{-1} and increases between 800-1000 cm^{-1}. Post-treatment PAT-52 and PAT-73 cells saw comparable changes to each other across targeted inhibitors but differed with nivolumab. Post-nivolumab PAT-52 cells had increased intensities across protein bands 843, 917, 924, 958, and 968 cm^{-1}, whereas PAT-73 showed minor changes, reflecting its clinical non-responder status to the inhibitor.

Comparison of persistent cell spectra with targeted inhibitor spectra suggested the presence of remnant inhibitors. Increased intensities of post-bemcentinib cells at 1156 and 1550-1600, and a discontinuity at 1615 cm^{-1}, coincided with major bemcentinib bands (Supplemental Figure 3). Similarly, a subset of post-cabozantinib cells, isolated by Leiden clustering, exhibited pronounced features at 1388, 1439, 1482, and 1611 cm^{-1}, likely corresponding to major cabozantinib peak assignments(Extended Data Figure 1). These findings seemed consistent with the half lives of cabozantinib (~120 hours) and bemcentinib (~150 hours)[47,48].

Our RF model retained a robust 94% accuracy across human samples, preserving general patient discernibility (Figure 4d). Within patients, classification generally performed better for those with relevant positively-expressed mutations (AXL+, BRAF+ in A375) than for low and wild-type expressions (AXL-, BRAF WT in SK-MEL-30) or nonresponsive (PAT-73) samples. Additionally, bemcentinib and cabozantinib-treated cell spectra appeared similar across patients, respectively, and as a result were more likely to be misclassified. Our findings demonstrate that Raman can effectively discern drug-resistant cells and comparative degrees of resistance in both mouse and human models across vastly different cell origins.

Patient melanoma sensitivity screening

Finally, we applied our methodology to develop drug determination classifiers for clinically-relevant patient samples. RF classifiers were chosen to evaluate resistance-sensitivity profiles for targeted therapies (bemcentinib, cabozantinib, dabrafenib), single-agent (nivolumab) and combination-agent (nivolumab + relatlimab) immunotherapy. We prospectively collected heavily-pretreated, resistant patients undergoing surgical resections as well as pretreatment specimens from patients planned for neoadjuvant therapy and followed clinical response. Our dataset encompassed five melanoma patients for training (minimum 500 spectra) and four

patients for testing (μ_{cells} = 522, min: 96, max: 1512). We augmented the inhibitor training set with commercial cell line spectra. Additionally, we collected spectra from multiple passages of select patients to examine passage drift changes. Given limited fresh tissue available prior to therapy exposure, we trained with at least two resistant and sensitive patients for each protocol when possible to maximize labeling power while moderately accounting for patient melanoma diversity (Supplementary Table 1).

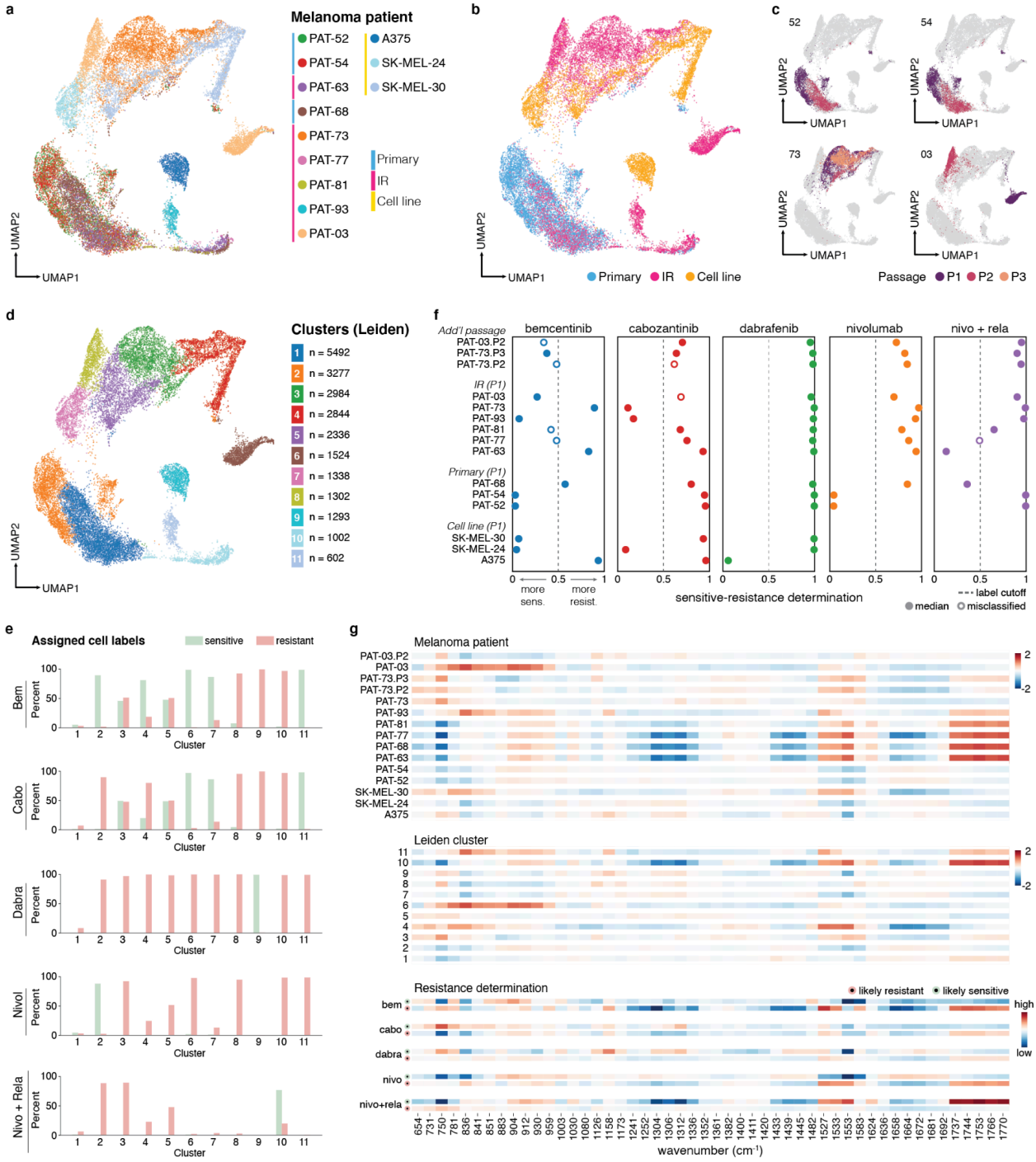

Figure 5. Analysis and response determination of patient-derived cell lines. A) UMAP embedding of Raman profiles from patient-derived cell lines and commercial human cell lines, where each point represents a cell spectrum, showing cellular heterogeneity across patient samples. B) UMAP colored by sample origin. C) UMAP highlighting cell spectra from select patients colored by passage number. D) UMAP embedding colored by Leiden clusters. E) Proportion of cell spectra within each Leiden cluster labeled resistant or sensitive across drugs of interest. F) Response determinations for patient-derived cell lines (seen and unseen by our ML model) across targeted and immunotherapy regimes. Using a 0.5 cutoff boundary to label resistant and sensitive samples, 26 of 33 test drug-patient cases were correctly labeled. G) Spectral barcode of highly variant wavenumbers quantified by the median fold change across samples (top), Leiden clustering (middle), and higher (>0.8) and lower (<0.2) resistance likelihood determined by our ML model (bottom).

UMAP visualization highlighted significant melanoma heterogeneity (Figure 5a). Primary tumor-derived cells were mainly consolidated in one region, whereas tumors derived from immunotherapy-refractory (IR) patients showed broader heterogeneity (Figure 5b). Some IR patient spectra (PAT-03, PAT-73) overlapped with commercial melanoma cell line spectra, suggesting biological similarities.

Additionally, we observed tumor compositional drift and cell population convergence across passages, marking phenotypic drift in metastatic progression (Figure 5c). UMAP showed later passages of several patients (PAT-52, PAT-54, PAT-63, and PAT-68) converging to a single grouping different from their initial passages (Figure 5c), with elevated intensities at 1658 and lowered intensities at 750, 1312, and 1583 cm^{-1} (Extended Data Figure 2,3). Meanwhile, later passages of PAT-73 and PAT-03 localized within prior passages or near melanoma cell lines. Single-cell RNA sequencing (scRNA-seq) on these later passages revealed near homogenous cell populations with fibroblast-like marker genes for PAT-52, PAT-54, PAT-63, and PAT-68, whereas PAT-73 and PAT-03 showed fewer fibroblast-like features, consistent with our spectral observations (Extended Data Figure 4).

Leiden clustering (resolution=0.5) further identified cell type clusters largely independent of patient origin, in agreement with our scRNA-seq observations (Figure 5d, Extended Data Figure 5). Cluster 1 had a fibroblast-like profile, while clusters 3-5 contained mixtures of patient and commercial tumor cells (Figure 5d). Interestingly, when mapping patient response data (determined by clinical and cell viability assessment) to these clusters (Figure 5e), we found many clusters exhibited homogenous resistance labeling, with patients grouped in the same cluster tending to share similar drug response profiles. For example, PAT-52 and PAT-54 cells mostly resided in cluster 2 with identical resistance across cabozantinib, dabrafenib, and the combo nivolumab + relatlimab (Supplementary Table 1). Similarly, PAT-63 and PAT-68 cell spectra mainly resided in cluster 10, with resistance to all drugs except our combination regimen. These observations suggest Raman profiling may identify similarly responding cells and provide insight into selecting second line treatments.

We developed a set of classifiers to determine patient resistance likelihoods based on their Raman profiles. Our model first trained on passage 1 binary labels and predicted single-spectrum resistance probabilities. We then calculated a likelihood range based on the aggregated probabilities of spectra subsets (termed “mini patients”) randomly drawn from a

patient superset – an approach which effectively captures the significant intratumoral heterogeneity present in metastatic melanoma. Using a 0.5 threshold and 25,000 mini patients per patient, our model correctly classified 79% (26/33) of patient-drug combinations (Figure 5f). Our worst performing model (bemcentinib, 3/7 patients) had most misclassified determinations residing around the cutoff threshold. Adjusting the 0.5 threshold to an optimized labeling cutoff across each treatment further improved our patient-drug response accuracy to 91% (30/33) (Extended Data Figure 6).

Interestingly, our model showed some differences in drug resistance associated with passage number. For example, PAT-03 resistance likelihood to bemcentinib increased with passage number, while PAT-73 resistance likelihood to bemcentinib decreased with passage number. Cell viability data similarly reflected the higher values in later passages of PAT-03 and lower values in later passages of PAT-73.

Spectral barcodes created from the fold change of fifty highly variant peak assignments were compared across patient samples, Leiden clusters, and cells labeled highly resistant (likelihood >0.8) or sensitive (likelihood <0.2) (Figure 5g). Patient spectral barcodes clearly distinguished common band “expressions”. Notably, barcodes associated with highly-resistant and sensitive cases revealed differentially expressed intensities distinct across treatments, with the most significant wavenumbers at 750, 836, 1527, 1553, and 1737-1770 cm^{-1}. Cross examination of these barcodes provided a more comprehensive assessment of patient response. For example, comparing patient barcodes at the cutoff determination for bemcentinib (PAT-77, PAT-81) with bemcentinib-response barcodes and cluster 10 (predominantly bemcentinib-resistant) would adjudicate these borderline cases as likely resistant. On the other hand, PAT-77 would remain misclassified for our combination immunotherapy through cross examination, indicating an upper bound on improvement due to patient training set size. With a larger patient set, this two-stage evaluation approach could further improve second-line therapy selection assessment and reduce toxicity risk and adverse effects associated with ineffective treatments[49].

Discussion

In summary, we present the potential of Raman spectroscopy in combination with machine learning as a powerful omics tool for single-cell profiling and therapeutic screening. We identify biochemical functional phenotypes discerning melanoma cell plasticity and macrophage polarization. We observe biochemical bands indicative of drug resistance and find recurrent bands shared by residual cells invariant of sample source. We illustrate our analysis framework potency through a scalable, prognostic model capable of evaluating targeted therapy and immunotherapy resistance for clinically relevant melanoma samples. By combining clinical and *in vitro* outcomes, our predictors correctly assign resistance likelihood to a majority of unseen patient-drug combinations without necessitating post-drug characterization.

Although our model is promising, several limitations remain to be addressed to improve predictive performance. Our small patient training set likely introduced patient-dependent biases during learning stages, while our resistance-imbalanced dataset limited sensitive-labeling confidence. Expanding the training library, notably with untreated pre-therapy patients and

through collaborative efforts across high-volume centers, would better capture melanoma diversity and spectral patterns faithful to treatment. Larger training libraries would further enable the utilization of artificial neural networks. Additionally, our binary labeling scheme oversimplified the complex TIME response, and further explorations of more complex combination immunotherapy selections may necessitate 3D organoid modeling[50,51]. We expect our model efficacy to improve with more complex labeling and consistent retraining with evolving demarcations. Finally, our learning architecture naively assumed equal significance across patient spectra regardless of inhibitor relevance. Future considerations could incorporate weighted selection of patient spectra based on cluster importance, cell type assignment, and drug mechanism targets.

Our Raman-based omics platform can be built upon to increase lab and clinical utility. Incorporation of surface enhanced Raman strategies (SERS) can enable higher profiling throughput at subcellular spectral resolution. Utilization of dielectric-based nanostructures (e.g. metasurfaces) may boost Raman scattering many orders of magnitude while localizing interactions at the cell membrane, minimizing cell damage and better facilitating cell characterization[52,53]. Extending our approach to spatially resolved profiling can offer a powerful tool for organoid, tumor, and tissue screening, greatly improving our understanding of the TIME and cell-cell interactions[39]. With advanced deep learning models, fine-tuned hyperparameters, and contemporary preprocessing pipelines, a spatial framework would provide a more clinically-faithful and readily accessible assay.

Raman-based omics promises a rapid, label-free screening platform to forecast melanoma and other heterogeneous tumors response to precision therapy. As a non-destructive optical approach, our complementary method resolves many of the challenges faced by traditional omics screening and may easily integrate with other modalities (e.g. single-cell sequencing). Combined with other omics methods and novel molecular imaging methods such as iFRET, multichannel stratagems may provide a more comprehensive understanding of the TIME and biomolecular changes underpinning therapeutic response[54].

Methods

SAMPLE PREPARATION

Cell lines and culture conditions of human and mouse melanoma cancer cells

Human (A375, SK-MEL-24), mice melanoma cancer cells (YUMM1.7, YUMMER1.7, B16-F10) and mice macrophage cell line (RAW 264.7) were acquired from the American Type Culture Collection (ATTC, Manassas, VA). Additionally, SK-MEL-30 human melanoma cell line was acquired from DSMZ-German collection (Braunschweig, Germany), and LN6-Engleman mouse cell line was procured from the Engleman Lab (Stanford, CA). Cells were cultured in complete cell culture growth medium including RPMI (Gibco, Grand Island, NY) supplemented with 10% fetal bovine serum (Corning, Woodland, CA) at 37°C in an incubator supplied with 5% CO_2. Media was changed at least twice a week.

Human melanoma patient-derived cell lines and culture

Human melanoma tissue specimens were procured from patients undergoing treatment, following the approved tissue collection protocol (IRB 65607) established by the Stanford University Institutional Review Board. All patients provided written informed consent. Samples were collected from adult individuals of both genders. All surgical specimens were confirmed to be melanoma prior to processing. Melanoma tissues were collected in RPMI media and transported to lab on ice and rinsed with DPBS (Gibco) and removal of excess connective and vascular tissues. Subsequently, tissues were finely minced using a sterile scalpel and collected in the tube. After centrifugation (5 min at 4°C, 400 g) the cell pellet was resuspended in DMEM/F12 (Invitrogen, Waltham, MA), 12 mM HEPES (Invitrogen), 1% GlutaMAX (Invitrogen), 10% fetal bovine serum (FBS), supplemented with 9 μM ROCK (Y-27632) inhibitor (Selleckchem, Houston, TX) and 1% penicillin/streptomycin (Invitrogen). Cells were seeded in a cell culture dish and kept at 37°C and 5% CO_2 in an incubator. Once they reached 65-70% confluence, cells were detached with TrypLE Express (Gibco), centrifuged (5 min at 4°C, 400 g) and seeded in 6 well plates at a density of $1x10^6$ cells per well for drug treatment. Cells were tested with Bemcentinib (MCE, Monmouth Junction, NJ) at 8μM, Cabozantinib (MCE) at 9.5 μM, Dabrafenib (Selleckchem) at 5 μM, Nivolumab (Selleckchem) at 6 μM, and Nivolumab + Relatlimab (MCE) at 6 μM + 7 μM. For select patient samples, cells were further partitioned for fixation protocols used in Raman data acquisition and for preparation for single-cell transcriptomic sequencing.

Chemically induced macrophage polarizations

Mouse RAW264.7 macrophages were cultured in RPMI media supplemented with 10% fetal bovine serum. For differentiation, RAW264.7 cells were stimulated with LPS (100 ng/ml) for 24 hours to obtain M1 polarization macrophages and IL-4 (20 ng/ml) and IL-13 (20 ng/ml) for 24 hour to obtain M2 polarizations. Non-stimulated (M0) macrophage cells served as controls in experiments. For each polarization state, plasticity changes were quantified by FACS and microscopic images.

Drug response screening

Human melanoma cancer cell lines (A375, SK-MEL-24, and SK-MEL-30) and murine melanoma cancer cell lines (YUMM1.7 and YUMMER1.7) were cultured in RPMI supplemented with 10% FBS. Cells were cultured at 37°C in a humidified CO2 incubator at 5% CO2. Upon reaching 75-80% confluency, cells were trypsinized (Trypsin-EDTA, Gibco) for 5 min at 37°C, collected in suspension in a 15 mL tube, and centrifuged at 400 g for 5 minutes at 4°C. The supernatant was removed, and the cell pellet was resuspended with 1 mL RPMI complete media. Cells were counted and plated at a density of $1x10^6$ cells/well into a 6-well plate and placed overnight in an incubator for adherency. Cells were then treated with desired inhibitors with varying concentrations for 24 hours. Inhibitor concentrations for all samples can be found in Supplementary Table 2. Duplicate wells were used for both treated and untreated cells. Plates were incubated for 24 hours. Dead cells along with the drug media were removed, and cells were trypsinized for 5 minutes, collected into 15 mL tubes, and centrifuged at 400 g for 5 minutes. After supernatant removal, cells were resuspended into 1 mL of media, and cell viability was assessed with Trypan blue assay. Hits were identified using a threshold of 65-70% inhibition of cell viability.

Cell fixation and and placement on gold-coated slides

Melanoma cancer cells were cultured until 65-70% confluency. Media was aspirated, and the cells were washed with 5 mL of PBS. After removal of media, 3 mL of 0.25% trypsin-EDTA was added to the culture flask and incubated at 37°C at 5% CO_2 for 5-7 min. After incubation, RPMI + 10% FBS was added to quench the trypsin reaction, and the cell suspension was collected into a 15 mL centrifuge tube. The tube was spun for 5 minutes at 400 g, and the supernatant was aspirated. Next, 1 mL of 4% paraformaldehyde was added, and the solution was mixed gently and incubated at room temperature for 10 minutes. After incubation, the tube was centrifuged for 3 minutes at 400 g at 4ºC before supernatant removal. The cell pellet was resuspended with an additional 1 mL PBS and centrifuged for 3 minutes at 400 g. The supernatant was aspirated, 50 uL of PBS was added, and the solution was gently mixed. Based on cell concentration, 1-5 uL of cell solution was drop casted on a gold-coated slide (~195 nm Au, 5 nm Ti, 1 mm glass) and air dried for 5-10 minutes prior to Raman acquisition.

Sample preparation of targeted inhibitors for Raman measurements

Powders of high purity (>99.9%) bemcentinib, cabozantinib, and dabrafenib were each thoroughly mixed with 3 uL of 1x PBS with a pipette. 2 uL of our mixture was dropcast on a gold-coated slide and air dried for 5-10 minutes prior to Raman acquisition.

scRNA-seq cell and library preparation

Patient-derived melanoma cell lines were trypsinized for 5 minutes, collected into 15 mL tubes, then spun down at 400 g for 5 min at 4°C. After removing the supernatant, the cells were resuspended in 1 mL of PBS with 0.5% BSA. Live and dead cells were visualized and counted using Trypan blue. If over 40% of dead cells were present, the sample was spun down at 400 g for 5 min at 4°C and subject to the dead cell removal kit (Miltenyi Biotec, 130-090-101). Finally the samples were spun down at 400 g for 5 min at 4°C and resuspended in 500 µL - 1 mL of PBS for a final concentration of 1000-1,500 cells/µL for a target cell recovery of 20,000 cells. For the characterization studies, library preparation was performed using Chromium GEM-X

Single Cell 3' Reagent Kits v4 (10X Genomics). Library conversion was then done using Singular Genomics Library Compatibility Kit (Singular Genomics). Libraries were sequenced on the Singular Genomics G4 sequencer, using 100 cycle F3 flow cells (Singular Genomics), with two lanes per library at 28/90 paired end.

SPECTRAL MEASUREMENTS

Raman data acquisition

Raman spectra on the dried samples were acquired using a confocal Raman spectrometer (Horiba LabRAM, Longjumeau, France) at 532 nm excitation with a 100x 0.6 NA objective at five second integration times. Using a 600 gr/mm grating, the spectral acquisition range acquired was 500-2000 cm^{-1}. All spectra, unless otherwise stated, were acquired with 100% power output of ~5.4 mW with a nominal spot size of ~2.1 µm. Spectra for murine sample B16-F10 and human samples SK-MEL-30 (control) and PAT-73 (bemcentinib) were collected at both 100% and 50% power using an integrated ND filter. Spectra for murine samples YUMM (cabozantinib, dabrafenib, nivolumab) were collected at both 25% and 50% power. Spectra were acquired via a rectangular grid map at 20 µm spacings between point measurements, or via a point-by-point selection per window region to minimize cell measurement duplicates. At least 1000 spectral measurements were acquired for each sample prior to data preprocessing. Spectra for targeted inhibitors were acquired with 25% power for dabrafenib and bemcentinib and at 100% power for cabozantinib.

Data preprocessing

Spectra were first filtered by an intensity count threshold to remove detector saturated measurements. Unprocessed Raman spectra were then despiked using a modified Whitaker-Hayes method to remove cosmic rays and spiked pixel regions on the CCD[55]. Upon despiking, spectra were denoised via wavelet thresholding. The python package skimage was used to perform our smoothing, and BayesShrink was chosen as our wavelet coefficient threshold selection method. Following our spectral smoothing, a baseline correction was applied using a combination of polynomial fitting (4th order) and adaptive iteratively reweighted Penalized Least Squares (airPLS)[56]. The correction method was implemented using the python packages PeakUtils and BaselineRemoval[57]. Each baseline-subtracted spectrum was internally normalized by replacing the intensity of each wavenumber with the standard score, calculated from the mean and standard deviation of the intensities in the spectrum, to enable cross-spectrum comparisons. The biological fingerprint region of 600-1800 cm^{-1} of the processed spectra was isolated for analysis. Off-cell measurements from grid mapping, stage translation drifts, and background mediums and poor-quality spectra characterized by high background to cell signal intensities were filtered utilizing a combination of one-class support vector machines and major biological bands z-scores for all datasets. The set of one-class support vector machines (SVMs, sklearn) was trained using spectra from relevant backgrounds (gold slide, phosphate-buffered saline, supernatant, polystyrene). In total, 8,095 cell spectra were utilized for murine TIME cell differentiation, 3,594 cell spectra for macrophage polarization, 9,937 cell spectra for murine drug response, 33,921 cell spectra for human drug response, and

23,994 cell spectra for melanoma resistance determination. Visualization of our preprocessing steps and background spectra can be found in Supplementary Figure 5.

DATA ANALYSIS

Spectral clustering and visualization

Preprocessed data were subjected to linear dimensionality reduction by PCA (sklearn) to reduce the feature size to a set of principal components explaining ≥95% of the dataset variance. The transformed dataset aided in visualization and in certain cases, improved classification runtimes. Manifold learning (UMAP, umap and Scanpy)[58,59] was applied to the PCA-reduced dataset to visualize the samples in a two-dimensional embedding, and hyperparameters random_seed=42, n_neighbors=25, min_dist=0.5, spread=1, n_epoch=500 were used across all datasets, with adjustments of the following: min_dist=0.3, spread=2 for murine cell differentiation described in Figure 2b; n_neighbors=30 for mice drug response, min_dist=0.3 for human drug response, and min_dist=0.3, spread=3 for patient data. Effects of hyperparameters to UMAP embedding are highlighted in Supplementary Figure 6. Leiden clustering[60] (Scanpy) with resolution 0.3 (human response) and 0.5 (patient dataset) was used to examine spectral differences among clusters. Heatmap analysis was performed by first shifting our dataset by a constant c, where c is the value needed to raise our minimum value to nonzero. After, the median value of the wavenumber features were determined from our control group. Median was selected over arithmetic mean for improved robustness against dissimilar group distributions[61]. In the case of the drug screening assay, the untreated cells served as control. Finally the fold change was determined for each sample through the log2 of the ratio between sample features and the control group. Log2 was chosen such that a two fold increase (doubling of quantity) resulted in a log2 fold change of +1 whereas a two fold decrease (halving of quantity) resulted in a log2 fold change of -1. All differential “expression” heatmaps were color bound with a vmin=-2 and vmax=2, representing a ±4-fold change. Wavenumber selections for the differential intensity heatmaps were either determined from the top wavenumbers affecting classification accuracy by perturbation calculations (see feature importance section below) or by the combination of most prominent peak selection in the average spectra (SciPy) and highest variant wavenumbers using Wilcoxon rank-sum (Scanpy).

Spectral barcodes

Spectral barcodes were generated from averaging the log2 fold change (differential intensity) of 500 spectra randomly selected within a relevant spectral set. The top 50 variant wavenumbers were integrated to create Raman profile spectral barcodes. For high-likelihood resistant and sensitive barcodes, the spectral set was constructed by filtering single cell spectra with predicted probabilities of >0.8 and <0.2 from each of the drug determination classifiers, respectively. Barcodes were color bound symmetrically with a ±0.5 for bemcentinib and cabozantinib, ±0.75 for nivolumab, and ±1 for dabrafenib and nivolumab + relatlimab to maximize comparability across treatments and reduce individual patient outliers and label imbalance associated with our limited patient dataset.

Spectral classification

A random decision forest (sklearn) was utilized to classify our samples. Optimal hyperparameters were determined by grid search (sklearn) across discrete parameter space with stratified shuffle splitting and identical random seeds. PCA transformed spectra were used for classification, with a 10-split stratified k-fold cross-validation (sklearn) with shuffle=True and weights associated with classes were balanced based on labeling frequency to reduce overfitting and account for uneven datasets. The performance of the random forest model was evaluated by a confusion matrix.

Leiden cluster cell response labeling

For each Leiden cluster, the number of cells labeled resistant and sensitive was determined by examining the clinical and cell viability data. Cluster population proportions were then calculated relative to the total number of cell spectra assigned to the cluster, where the sum of resistant + sensitive + unlabeled cell spectra proportions = 1.

Feature importance

Raman wavenumbers importance were determined by analyzing the classification accuracy dropoff from spectra masking across all wavenumbers[62]. First, a 10-split stratified shuffle cross-validation (sklearn) was utilized with an 80:20 training:test split. Utilizing the random forest model discussed prior, we then determine the general classification performance as each wavenumber feature is perturbed with a Voigt profile of alpha=5, gamma=2 of the pre-transformed data for each test split. The average classification accuracy and standard deviation was then calculated for each feature. The Raman bands with the biggest effect on classification were selected by a descending sort of the largest peaks (SciPy) associated with 1-classification accuracy.

Construction and implementation of resistance determination model

A random forest multiclass classifier (sklearn) was constructed for each drug of interest using hyperparameters max_depth = 20, max_features = “sqrt”, n_estimators = 275. Hyperparameters were selected by grid searching on the nivolumab training dataset and utilized for remaining determination models. Additionally, class_weight=’balanced’ was used to account for imbalance training datasets. Spectra labels for patients were annotated as either 0 (sensitive) or 1 (resistant) based on clinical observations and in vitro cell viability assessments. Cell viability cutoffs for resistant or sensitive labels for targeted inhibitors was set at 70% and immunotherapy was set at 60%. Viability values falling near the cutoff boundary (±2%) were selected as sensitive over resistant. Commercial human cell lines and patients samples without added in vitro treatments were selected for our training and test datasets. Each training patient sample was required to have 500+ spectra. In summation, the first passages of patient samples PAT-52, PAT-54, PAT-63, PAT-73, PAT-93 and cell lines A375, SK-MEL-24, and SK-MEL-30 were utilized in our training set. Class probabilities from 0 to 1 as defined by class probabilities in our RF model were determined for each spectra, where values closer to 0 and 1 corresponded with more sensitive and more resistant, respectively. A binary label of resistant or sensitive could then be assigned based on a desired determination cutoff threshold for each drug protocol of interest. In our model, we chose 0.5 as our determination cutoff.

Aggregated patient response

For each patient, 25,000 mini patients were generated by grouping 100 cell spectra randomly selected using uniform weighting from the patient superset. For each spectra in a mini patient, the resistance probability for a drug was predicted using our pre-trained RFs, and the quantitative response (sensitive, resistant) of a mini patient was calculated by the mean of the spectra likelihoods. The response determination of the patient for each drug protocol was then assessed by examining the median, 5th, and 95th percentile of the distribution of mini patient responses.

scRNA-seq analysis

Data were aligned with cellranger 9.0.0 to reference genome GRCh38-2024-A[63]. Data were imported into python as anndata objects for further analysis using the Scanpy framework[59,64]. Preprocessing was performed on each sample individually. Cells with fewer than 100 unique genes or more than 10% mitochondrial counts were removed. Doublets were removed using the DoubletDetection package with Louvain clustering, 20 iterations, 1e-16 p-value threshold, and 0.5 voter threshold[65]. Integration was performed with scVI using the top 2000 highly variable genes[66–68]. The model was trained for 100 epochs. Leiden clustering was performed at resolution 0.9. Differential expression analysis was performed using the scVI differential expression module, and cells were manually annotated as tumor cells and fibroblast-like cells using canonical marker genes. One cluster that had a mixed gene expression profile was marked as unknown. The scANVI framework was then used for further integration using the scVI annotations as initial labels[69]. Leiden clustering was performed at resolution 1.0. Differential expression analysis was performed using the scVI differential expression module, and cells were manually annotated as tumor cells and fibroblast-like cells using canonical marker genes.

References

1. Chacon, A. C., Melucci, A. D., Qin, S. S. & Prieto, P. A. Thinking Small: Small Molecules as Potential Synergistic Adjuncts to Checkpoint Inhibition in Melanoma. *International Journal of Molecular Sciences* **22**, 3228 (2021).
2. Nikolaou, V., Tsimpidakis, A. & Stratigos, A. Cutaneous Adverse Reactions of Immunotherapy in Patients with Advanced Melanoma. *Cancers* **15**, (2023).
3. Atkins, M. B. *et al.* Combination Dabrafenib and Trametinib Versus Combination Nivolumab and Ipilimumab for Patients With Advanced BRAF-Mutant Melanoma: The DREAMseq Trial—ECOG-ACRIN EA6134. *Journal of Clinical Oncology* (2023) doi:10.1200/JCO.22.01763.
4. Tsimberidou, A. M., Fountzilas, E., Nikanjam, M. & Kurzrock, R. Review of precision cancer medicine: Evolution of the treatment paradigm. *Cancer Treat. Rev.* **86**, 102019 (2020).
5. Binnewies, M. *et al.* Understanding the tumor immune microenvironment (TIME) for effective therapy. *Nature Medicine* **24**, 541–550 (2018).
6. Grzywa, T. M., Paskal, W. & Włodarski, P. K. Intratumor and Intertumor Heterogeneity in Melanoma. *Transl Oncol* **10**, 956–975 (2017).
7. Wagner, E., Larijani, B. & Kirane, A. R. Predictive biomarkers for immune checkpoint inhibitor therapy in advanced melanomas. *Surg. Oncol. Clin. N. Am.* (2025) doi:10.1016/j.soc.2025.01.006.
8. Fan, J., Slowikowski, K. & Zhang, F. Single-cell transcriptomics in cancer: computational challenges and opportunities. *Experimental & Molecular Medicine* **52**, 1452–1465 (2020).
9. Baysoy, A., Bai, Z., Satija, R. & Fan, R. The technological landscape and applications of single-cell multi-omics. *Nat. Rev. Mol. Cell Biol.* **24**, 695–713 (2023).
10. Wen, J. *et al.* Detection and Classification of Multi-Type Cells by Using Confocal Raman

Spectroscopy. *Front. Chem.* **9**, 641670 (2021).

11. Zhang, L. *et al.* Raman spectroscopy and machine learning for the classification of breast cancers. *Spectrochimica Acta Part A: Molecular and Biomolecular Spectroscopy* **264**, 120300 (2022).
12. Ogunlade, B. *et al.* Rapid, antibiotic incubation-free determination of tuberculosis drug resistance using machine learning and Raman spectroscopy. *Proceedings of the National Academy of Sciences* **121**, e2315670121 (2024).
13. Qiu, X. *et al.* Raman spectroscopy combined with deep learning for rapid detection of melanoma at the single cell level. *Spectrochim. Acta A Mol. Biomol. Spectrosc.* **286**, 122029 (2023).
14. Zhu, C., Wei, Y. & Wei, X. AXL receptor tyrosine kinase as a promising anti-cancer approach: functions, molecular mechanisms and clinical applications. *Mol. Cancer* **18**, 1–22 (2019).
15. Zdżalik-Bielecka, D. *et al.* Bemcentinib and Gilteritinib Inhibit Cell Growth and Impair the Endo-Lysosomal and Autophagy Systems in an AXL-Independent Manner. *Mol. Cancer Res.* **20**, 446–455 (2022).
16. Graham, D. K., DeRyckere, D., Davies, K. D. & Earp, H. S. The TAM family: phosphatidylserine-sensing receptor tyrosine kinases gone awry in cancer. *Nat. Rev. Cancer* **14**, 769–785 (2014).
17. Lian, L. *et al.* VEGFR2 promotes tumorigenesis and metastasis in a pro-angiogenic-independent way in gastric cancer. *BMC Cancer* **19**, 1–15 (2019).
18. Wu, Y. *et al.* Combining the Tyrosine Kinase Inhibitor Cabozantinib and the mTORC1/2 Inhibitor Sapanisertib Blocks ERK Pathway Activity and Suppresses Tumor Growth in Renal Cell Carcinoma. *Cancer Res.* **83**, 4161–4178 (2023).
19. Hara, T. *et al.* Cabozantinib inhibits AXL- and MET-dependent cancer cell migration induced by growth-arrest-specific 6 and hepatocyte growth factor. *Biochem Biophys Rep* **21**, 100726

(2020).

20. Hanrahan, A. J. & Solit, D. B. BRAF Mutations: The Discovery of Allele- and Lineage-Specific Differences. *Cancer Res.* **82**, 12–14 (2022).
21. Ai, L. *et al.* Research Status and Outlook of PD-1/PD-L1 Inhibitors for Cancer Therapy. *Drug Des. Devel. Ther.* **14**, 3625–3649 (2020).
22. Tawbi, H. A. *et al.* Relatlimab and Nivolumab versus Nivolumab in Untreated Advanced Melanoma. *N Engl J Med* **386**, 24–34 (2022).
23. Qin, S. S. *et al.* Intertumoral Genetic Heterogeneity Generates Distinct Tumor Microenvironments in a Novel Murine Synchronous Melanoma Model. *Cancers* **13**, (2021).
24. Meeth, K., Wang, J. X., Micevic, G., Damsky, W. & Bosenberg, M. W. The YUMM lines: a series of congenic mouse melanoma cell lines with defined genetic alterations. *Pigment Cell Melanoma Res.* **29**, 590–597 (2016).
25. Reticker-Flynn, N. E. *et al.* Lymph node colonization induces tumor-immune tolerance to promote distant metastasis. *Cell* **185**, 1924–1942.e23 (2022).
26. Movasaghi, Z., Rehman, S. & Rehman, I. U. Raman Spectroscopy of Biological Tissues. *Appl. Spectrosc. Rev.* (2007) doi:10.1080/05704920701551530.
27. Naumann, D. FT-INFRARED AND FT-RAMAN SPECTROSCOPY IN BIOMEDICAL RESEARCH. *Appl. Spectrosc. Rev.* (2001) doi:10.1081/ASR-100106157.
28. Brauchle, E. *et al.* Raman spectroscopy as an analytical tool for melanoma research. *Clin. Exp. Dermatol.* **39**, 636–645 (2014).
29. Danciu, C. *et al.* A characterization of four B16 murine melanoma cell sublines molecular fingerprint and proliferation behavior. *Cancer Cell Int* **13**, 75 (2013).
30. Yakimov, B. P. *et al.* Melanin distribution from the dermal–epidermal junction to the stratum corneum: non-invasive in vivo assessment by fluorescence and Raman microspectroscopy. *Sci. Rep.* **10**, 1–13 (2020).
31. Huang, Z. *et al.* Raman spectroscopy of in vivo cutaneous melanin. *J. Biomed. Opt.* **9**,

1198–1205 (2004).

32. Hourani, T. *et al.* Label-free macrophage phenotype classification using machine learning methods. *Sci. Rep.* **13**, 1–14 (2023).
33. Feuerer, N. *et al.* Lipidome profiling with Raman microspectroscopy identifies macrophage response to surface topographies of implant materials. *Proceedings of the National Academy of Sciences* **118**, e2113694118 (2021).
34. Naumann, M. *et al.* Label-Free Characterization of Macrophage Polarization Using Raman Spectroscopy. *Int. J. Mol. Sci.* **24**, (2023).
35. Ribeiro, A. R. B. *et al.* Application of Raman spectroscopy for characterization of the functional polarization of macrophages into M1 and M2 cells. *Spectrochim. Acta A Mol. Biomol. Spectrosc.* **265**, 120328 (2022).
36. Xie, J., Wei, Y., Liang, X., Ma, C. & Su, X. In situ single-cell spontaneous Raman spectroscopy differentiates tumor-associated macrophages. *Sensors and Actuators B: Chemical* **417**, 136053 (2024).
37. Xue, L. *et al.* Tryptophan metabolism regulates inflammatory macrophage polarization as a predictive factor for breast cancer immunotherapy. *Int Immunopharmacol* **125**, 111196 (2023).
38. Wang, J. *et al.* UV-induced somatic mutations elicit a functional T cell response in the YUMMER1.7 mouse melanoma model. *Pigment Cell Melanoma Res.* **30**, 428–435 (2017).
39. Sigle, M. *et al.* Translating genomic tools to Raman spectroscopy analysis enables high-dimensional tissue characterization on molecular resolution. *Nat. Commun.* **14**, 1–16 (2023).
40. Abramczyk, H. *et al.* Aberrant Protein Phosphorylation in Cancer by Using Raman Biomarkers. *Cancers (Basel)* **11**, (2019).
41. Xie, Y., Zhang, D., Jarori, G. K., Davisson, V. J. & Ben-Amotz, D. The Raman detection of peptide tyrosine phosphorylation. *Anal Biochem* **332**, 116–121 (2004).

42. Nyakas, M. *et al.* AXL inhibition improves BRAF-targeted treatment in melanoma. *Sci Rep* **12**, 5076 (2022).
43. Foda, B. M. & Neubig, R. R. Role of Rho/MRTF in Aggressive Vemurafenib-Resistant Murine Melanomas and Immune Checkpoint Upregulation. *Int J Mol Sci* **24**, (2023).
44. Chacon, A. *et al.* Abstract PO029: Development of a translatable targeted therapy-resistant melanoma model. *Development of a translatable targeted therapy-resistant melanoma model* Preprint at https://doi.org/10.1158/2326-6074.TUMIMM20-PO029.
45. Holzgruber, J. *et al.* Type I interferon signaling induces melanoma cell-intrinsic PD-1 and its inhibition antagonizes immune checkpoint blockade. *Nature Communications* **15**, 1–16 (2024).
46. Chen, M., Bie, L. & Ying, J. Cancer cell-intrinsic PD-1: Its role in malignant progression and immunotherapy. *Biomedicine & Pharmacotherapy* **167**, 115514 (2023).
47. Lacy, S. A., Miles, D. R. & Nguyen, L. T. Clinical Pharmacokinetics and Pharmacodynamics of Cabozantinib. *Clin Pharmacokinet* **56**, 477–491 (2017).
48. Loges, S. *et al.* Bemcentinib as monotherapy and in combination with low-dose cytarabine in acute myeloid leukemia patients unfit for intensive chemotherapy: a phase 1b/2a trial. *Nat Commun* **16**, 2846 (2025).
49. Zhong, L. *et al.* Small molecules in targeted cancer therapy: advances, challenges, and future perspectives. *Signal Transduction and Targeted Therapy* **6**, 1–48 (2021).
50. Zhao, Z. *et al.* Organoids. *Nature Reviews Methods Primers* **2**, 1–21 (2022).
51. Wang, Q., Yuan, F., Zuo, X. & Li, M. Breakthroughs and challenges of organoid models for assessing cancer immunotherapy: a cutting-edge tool for advancing personalised treatments. *Cell Death Discovery* **11**, 1–13 (2025).
52. Zhang, Y. *et al.* From Genotype to Phenotype: Raman Spectroscopy and Machine Learning for Label-Free Single-Cell Analysis. *ACS Nano* (2024) doi:10.1021/acsnano.4c04282.
53. Romano, S. *et al.* Surface-Enhanced Raman and Fluorescence Spectroscopy with an

All-Dielectric Metasurface. *The Journal of Physical Chemistry C* (2018) doi:10.1021/acs.jpcc.8b03190.

54. Kirane, A. R. *et al.* Toward Functional Biomarkers of Response to Neoadjuvant Oncolytic Virus in Stage II Melanoma: Immune-Förster Resonance Energy Transfer and the Dynamic Tumor Immune Microenvironment. *JCO Oncology Advances* (2025) doi:10.1200/OA-24-00049.
55. Whitaker, D. A. & Hayes, K. A simple algorithm for despiking Raman spectra. *Chemometrics and Intelligent Laboratory Systems* **179**, 82–84 (2018).
56. Zhang, Z.-M., Chen, S. & Liang, Y.-Z. Baseline correction using adaptive iteratively reweighted penalized least squares. *Analyst* **135**, 1138–1146 (2010).
57. Haque, A. *Feature Engineering & Selection for Explainable Models: A Second Course for Data Scientists*. (Lulu.com, 2022).
58. Sainburg, T., McInnes, L. & Gentner, T. Q. Parametric UMAP Embeddings for Representation and Semisupervised Learning. *Neural Comput* **33**, 2881–2907 (2021).
59. Wolf, F. A., Angerer, P. & Theis, F. J. SCANPY: large-scale single-cell gene expression data analysis. *Genome Biology* **19**, 1–5 (2018).
60. Traag, V. A., Waltman, L. & van Eck, N. J. From Louvain to Leiden: guaranteeing well-connected communities. *Scientific Reports* **9**, 1–12 (2019).
61. Lötsch, J., Kringel, D. & Ultsch, A. Revisiting Fold-Change Calculation: Preference for Median or Geometric Mean over Arithmetic Mean-Based Methods. *Biomedicines* **12**, (2024).
62. Safir, F. *et al.* Combining Acoustic Bioprinting with AI-Assisted Raman Spectroscopy for High-Throughput Identification of Bacteria in Blood. *Nano Lett* **23**, 2065–2073 (2023).
63. Zheng, G. X. Y. *et al.* Massively parallel digital transcriptional profiling of single cells. *Nature Communications* **8**, 1–12 (2017).
64. Virshup, I., Rybakov, S., Theis, F. J., Angerer, P. & Alexander Wolf, F. anndata: Access and

store annotated data matrices. *Journal of Open Source Software* **9**, 4371 (2024).

65. Gayoso, A. & Shor, J. JonathanShor/DoubletDetection: doubletdetection v4.3.0.post1. doi:10.5281/zenodo.14827937.
66. Lopez, R., Regier, J., Cole, M. B., Jordan, M. I. & Yosef, N. Deep generative modeling for single-cell transcriptomics. *Nature Methods* **15**, 1053–1058 (2018).
67. Virshup, I. *et al.* The scverse project provides a computational ecosystem for single-cell omics data analysis. *Nature Biotechnology* **41**, 604–606 (2023).
68. Gayoso, A. *et al.* A Python library for probabilistic analysis of single-cell omics data. *Nature Biotechnology* **40**, 163–166 (2022).
69. Xu, C. *et al.* Probabilistic harmonization and annotation of single‐cell transcriptomics data with deep generative models. *Molecular Systems Biology* (2021) doi:10.15252/msb.20209620.

Acknowledgements

The authors are grateful to H. Balch, V. Dolia, H. Carr Delgado, L. Herndon, J. Hu, D. Omo-Lamai, E. Wagner, C. Luna, and Prof. B. Larijani for their insightful discussions. The authors also thank the Reticker-Flynn lab for their assistance with sample procurement. Select elements of Figures 1-3 were created with Biorender.com. J.A.D. is a Chan Zuckerberg Biohub – San Francisco Investigator and acknowledges funding from the Chan Zuckerberg Biohub San Francisco, as well as from the National Institutes of Health (NIH) under grant no. 1DPAI15207201. J.A.D. and A.K. acknowledge funding from the Stanford Cancer Institute (SCI) Innovation Award. B.O. was additionally supported by the Stanford Graduate Fellowship, the Stanford EDGE Fellowship, and the Stanford Bio-X Bowes Graduate Student Fellowship. J.A. acknowledges funding from the Stanford Transplant and Tissue Engineering (TTE) Center of Excellence. A.S. was additionally supported by the National Science Foundation (NSF) through the Graduate Research Fellowships Program. Part of this work was performed at the Stanford Nano Shared Facilities (SNSF), supported by the National Science Foundation under award ECCS-2026822.

Contributions

K.C., M.S., A.K., and J.A.D. conceived and designed the experiments. M.S., H.H., S.S., and J.C. contributed to commercial cell and patient sample culturing and preparation. K.C., B.O., and M.S. developed the experiment protocols. K.C., M.S., B.O., and A.S. contributed to sample preparation and performed the spectroscopy measurements. K.C. and A.S. conducted the scanning electron microscopic characterizations. M.S. and H.H. conducted the cell viability measurements. M.S., H.H., S.S., and J.C. carried out the immunofluorescence and optical microscopic characterizations. M.S., H.H., A.G. contributed to library preparation and performed the single-cell sequencing. K.C. and J.A. analyzed the collected experimental data. N.V., F.S., and J.G. assisted in the development of the feature importance and classification workflow. A.S. assisted in the development of the Raman spectral preprocessing pipeline. J.G. assisted in the development of the outlier removal protocol. D.D. assisted in the single-cell sequencing analysis. K.C., M.S., J.A., J.G., D.D., A.K., and J.A.D. contributed to the interpretation of the results. All authors helped shape the research, analysis, and contributed to the manuscript. A.K. and J.A.D. conceived the idea and supervised the project, along with D.D. on relevant portions of the research.

Data and code availability

The data that support the findings in the work are available in the article and the supplementary information file, and are available from the corresponding authors on reasonable request. The source code for the analysis and visualization in this study is available from the corresponding authors on reasonable request.

Extended Data Figures

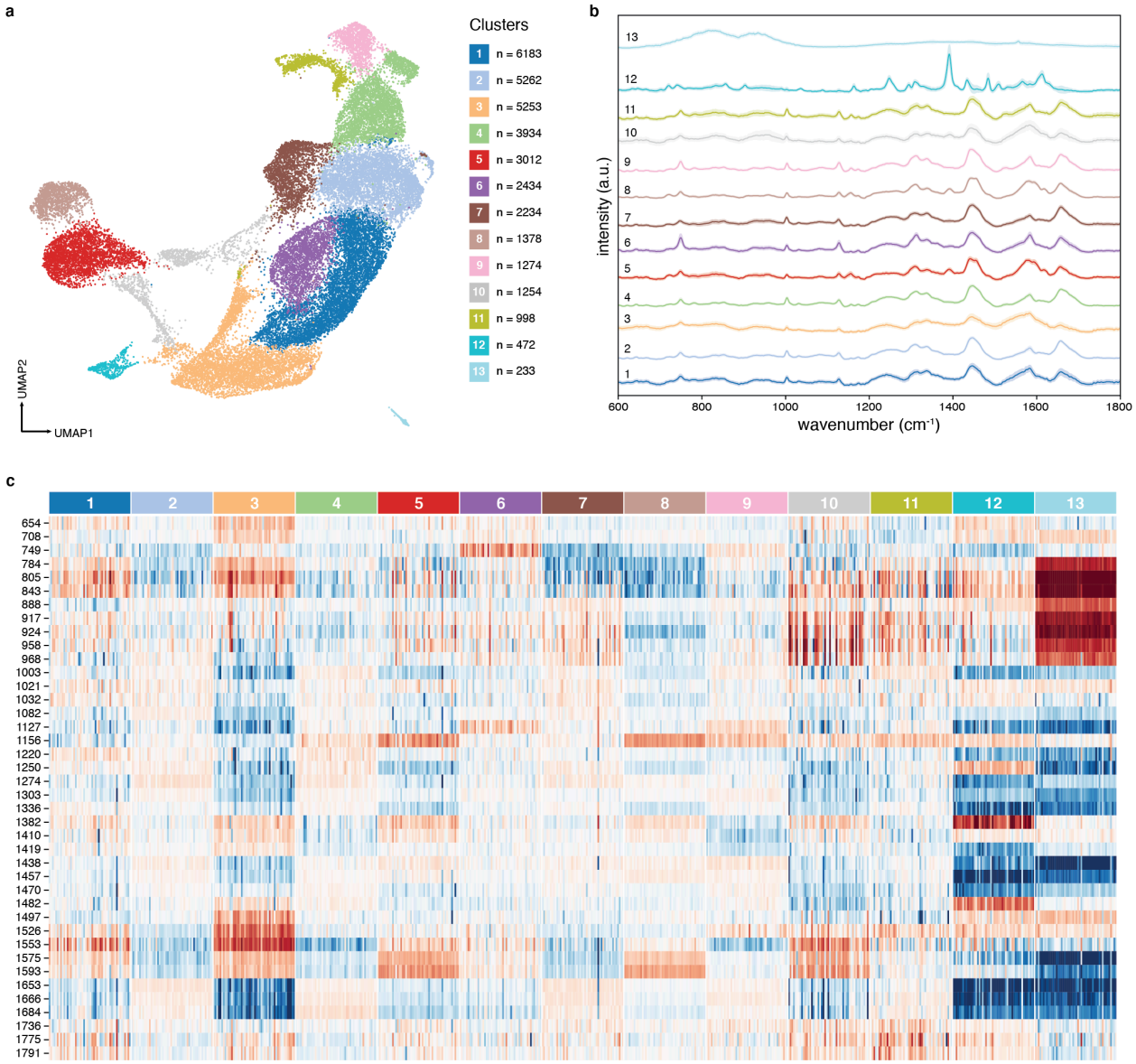

Extended Data Figure 1. Leiden clustering of human samples. A) UMAP embedding of Raman profiles from human melanoma response dataset grouped by Leiden clustering. Hyperparameters selected were nearest neighbors = 25, minimum distance = 0.3, number of epochs = 500, and Leiden resolution = 0.3. B) Mean normalized spectra and ±1 standard deviation across each Leiden grouping. Note, cluster 13 shows typical spectra from our substrate, while cluster 12 shows major bands found in spectra observed in cabozantinib. C) Differential wavenumber intensities of the median fold change across Leiden clusters showing distinct Raman “expression” for each cluster.

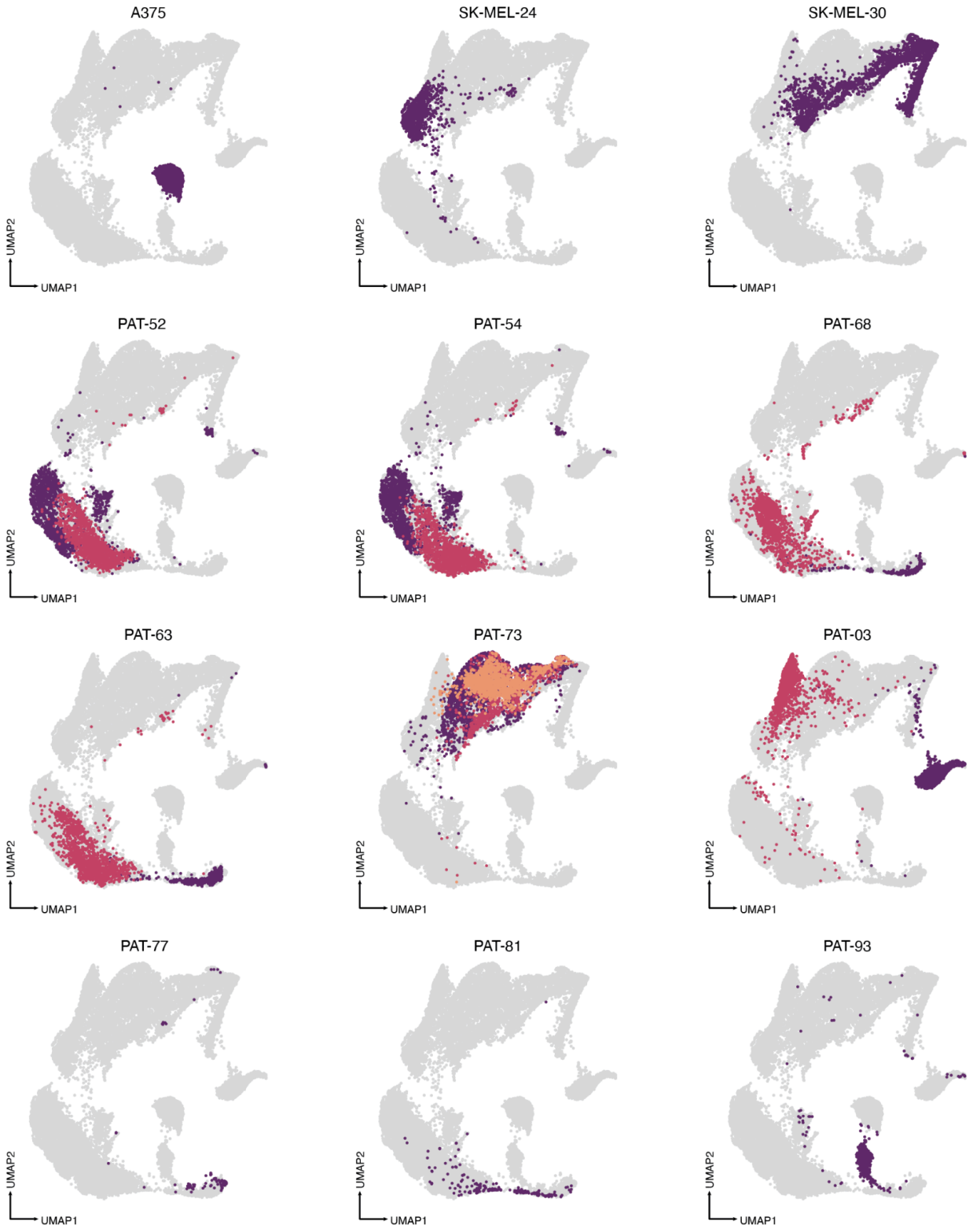

Extended Data Figure 2. Passage to passage variations for select patient samples. UMAP embedding of Raman profiles from patient melanoma and commercial cell lines. First passage is colored purple, second passage colored red, and third passage, if applicable, is colored orange. Two passages were analyzed for all patient samples

above, except for PAT-73 in which three passages were analyzed. Commercial cell lines are represented in the first row, primary tumors in the second, and immunotherapy-refractive patients in the remaining rows.

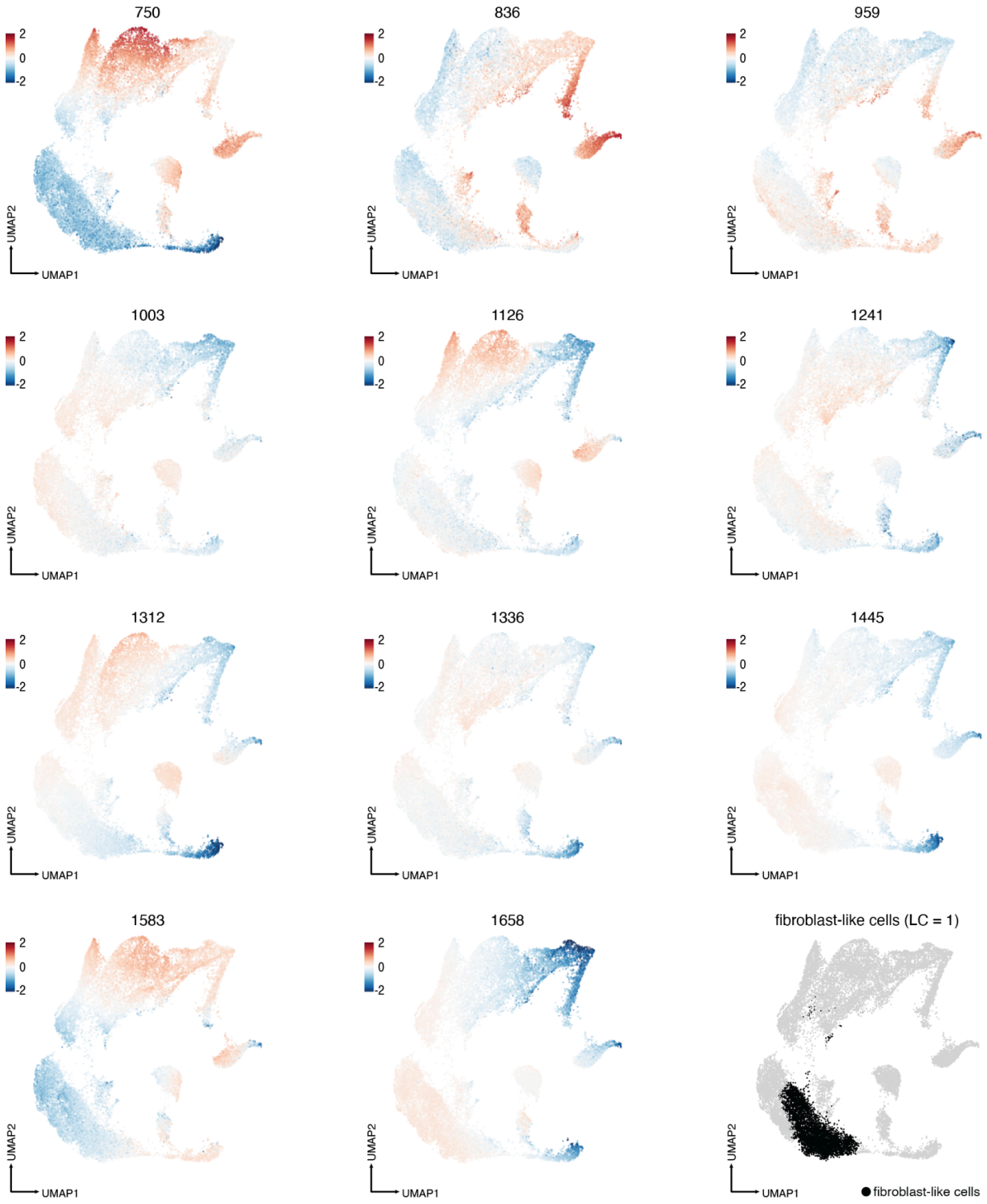

Extended Data Figure 3. Raman intensity fold change levels for patient samples by UMAP. Median fold change across select highly variant wavenumbers for our patient dataset, showing elevated or reduced "expression" across localized regions in latent space. Fibroblast-like cell profiles (cell spectra highlighted in black in the last subplot and corresponded to Leiden grouping 1) had elevated "expressions" across 1658 and reduced "expressions" across 750, 1312, and 1583 cm^{-1}.

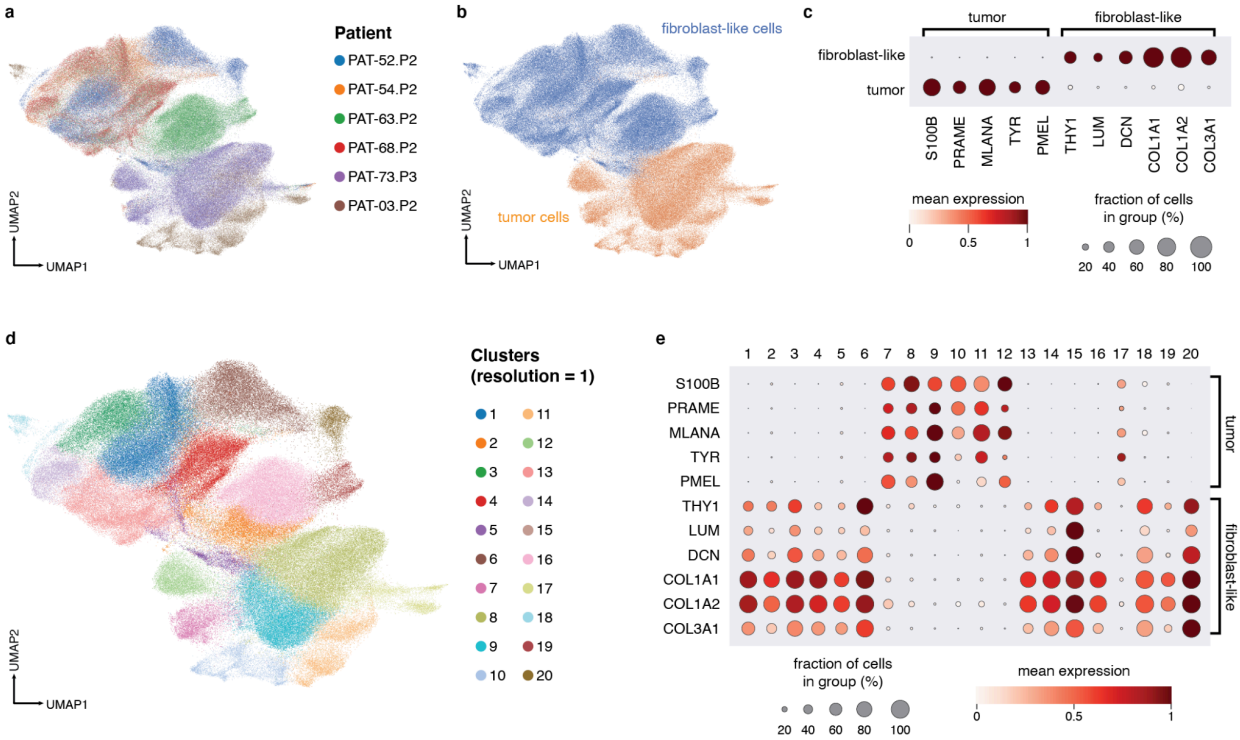

Extended Data Figure 4. Single-cell RNA sequencing of patient melanoma samples. Latest passages from samples PAT-52, PAT-54, PAT-63, PAT-68, PAT-73, and PAT-03 were sequenced. A) Transcriptomic UMAP colored by patient. B) UMAP colored by cell type based on canonical marker genes. C) Dotplot of marker genes associated with tumor-like and fibroblast-like features. D) Leiden clustering at resolution 1.0. E) Dotplot of marker genes grouped by Leiden cluster. We observe bimodal distribution in the expression of these markers.

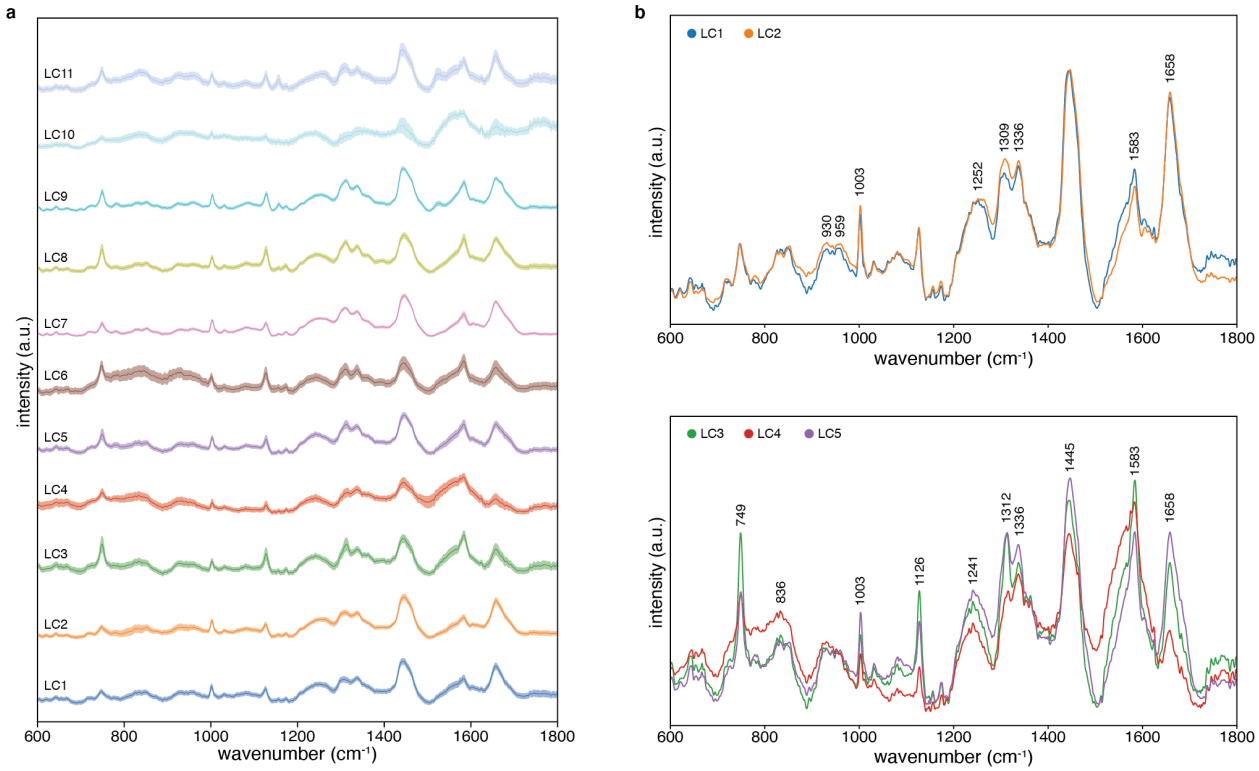

Extended Data Figure 5. Leiden clustering for human cell lines and patient samples. A) Mean normalized Raman spectra and corresponding ±1 standard deviation of cells residing in each Leiden cluster (resolution = 0.5) from Figure 5a. B) Spectra comparison between cluster 1 and 2, highlighting differences between fibroblast-like cells (LC1) and tumor cells (LC2). C) Spectra comparison betweens clusters 3-5, highlighting large phenotype heterogeneity across tumor cells.

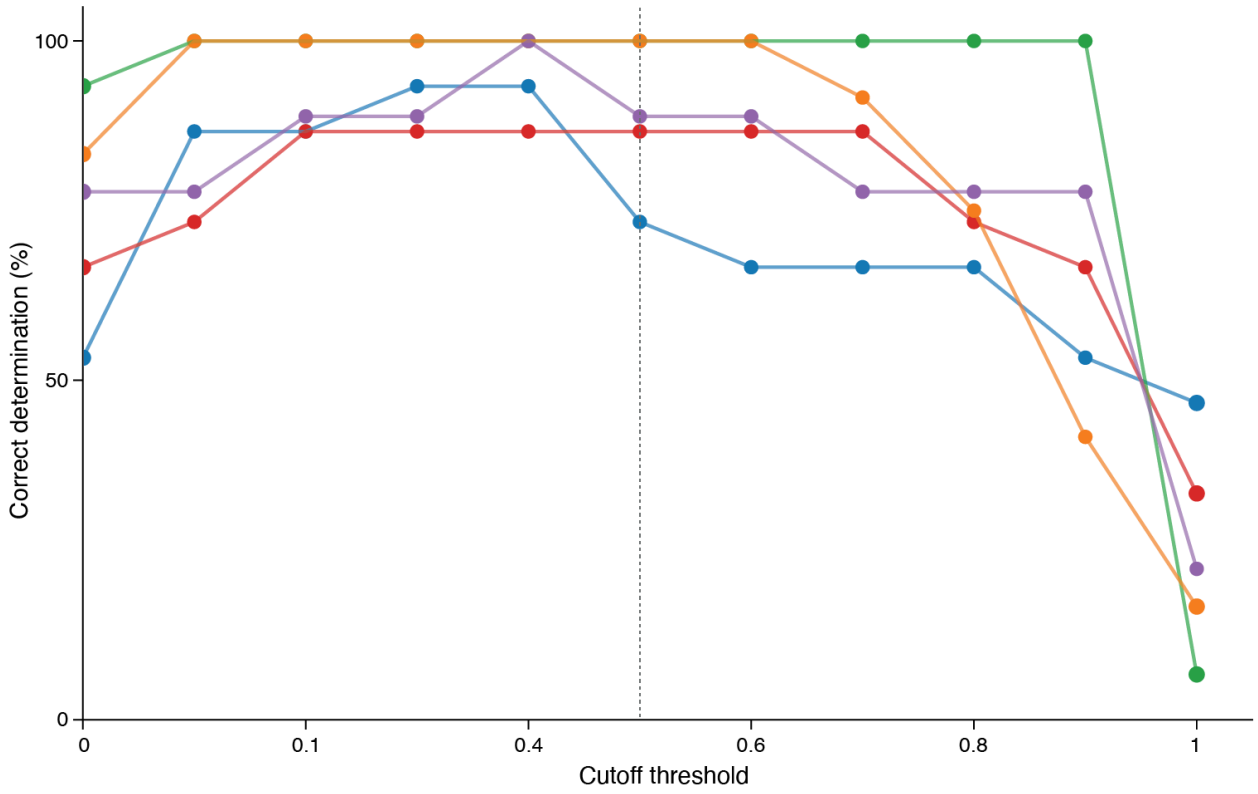

Extended Data Figure 6. Response determination accuracy vs. threshold selection. Examination of response determination accuracy of our prediction models across our patient samples as we vary the cutoff threshold (designating resistant and sensitive labels) of the median mini patient response. Assessment accuracy benchmarked against clinical outcomes and *in vitro* cell viability was determined for each drug classifier at 0.1 cutoff intervals. A 0.5 cutoff (dotted, grey line) was selected for all drugs of interest in our main analysis. For cabozantinib (red), dabrafenib (green), and nivolumab (orange) classifiers, the chosen cutoff threshold of 0.5 for our analysis provided the highest assessment accuracy. For bemcentinib (blue) and nivolumab + relatlimab (purple) classifiers, better assessment accuracies were found at lower cutoff values.

Supplementary Figures

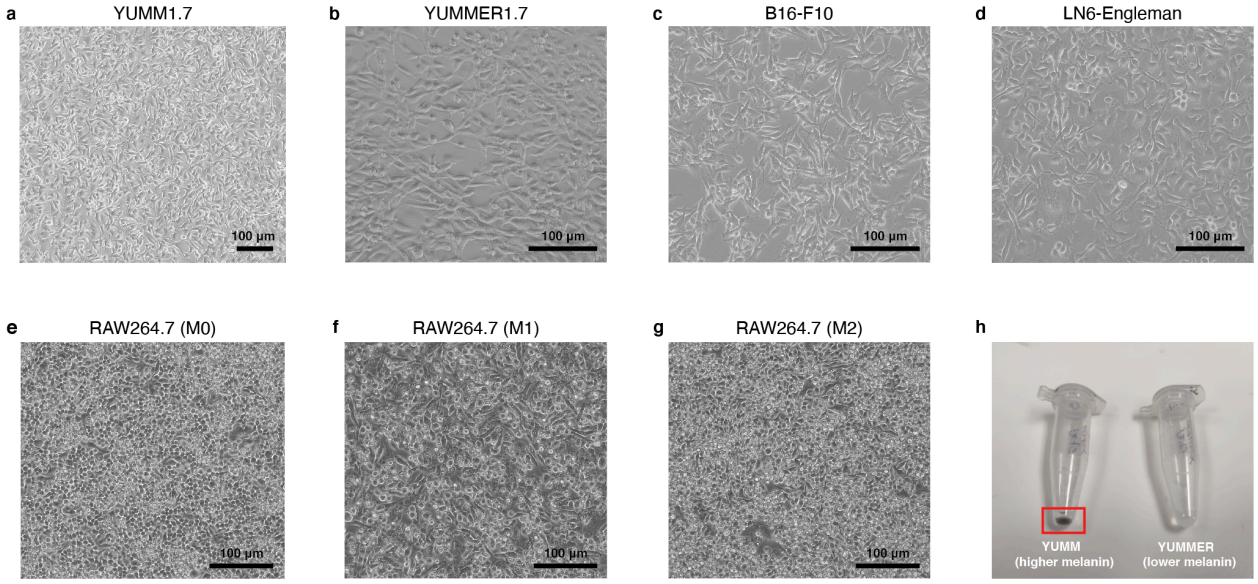

Supplementary Figure 1. Bright field images of mouse cells. A-G) Brightfield images of live murine cell lines. Images highlight morphological differences associated across cell types in cancer and immune cells and functional phenotypes in polarization states. Scale bar, 100 µm. H) Image of YUMM1.7 and YUMMER1.7 cell lines highlighting contrast in melanin pigmentation (higher melanin in the left tube highlighted with a red box), which was captured in our Raman analysis.

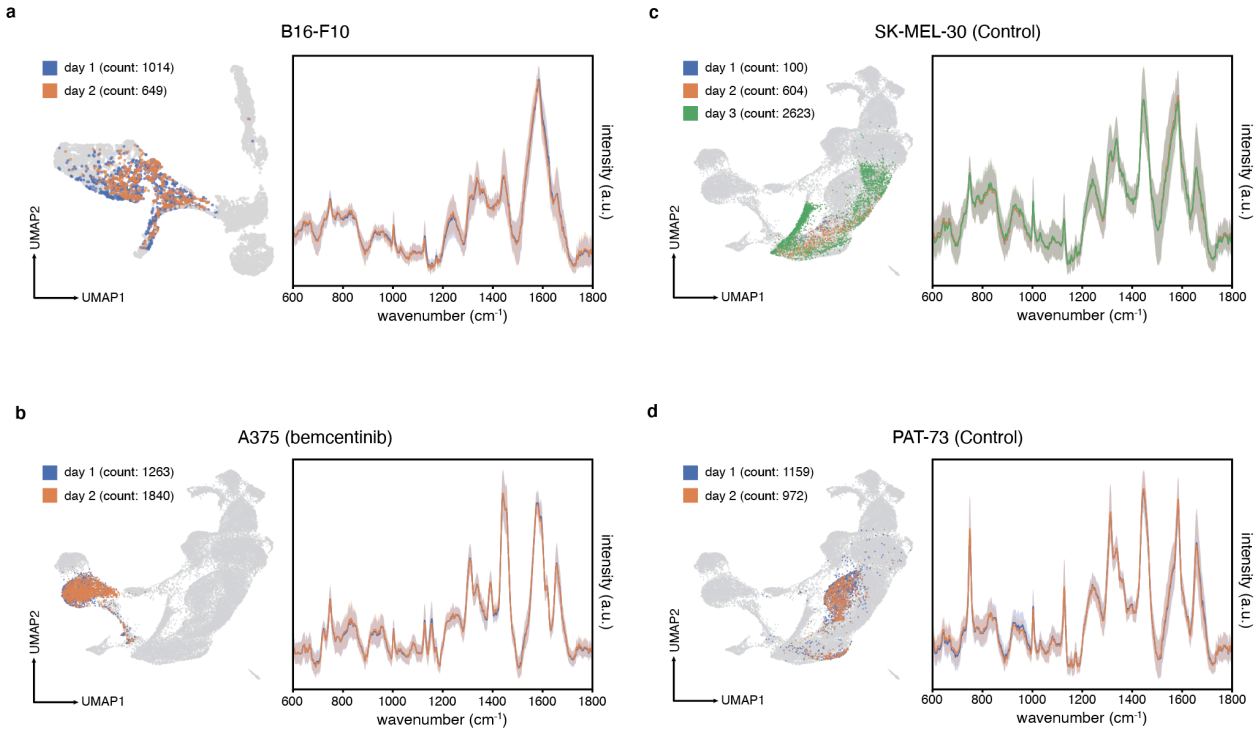

Supplementary Figure 2. Day to day variations in Raman spectra acquisition. Select mouse cell lines and human patient-drug treatment samples were measured across multiple days to examine spectra variability relating to sample preservation, environmental fluctuations, and instrumentation inconsistencies for (a) B16-F10, (b) A375-bemcentinib, (c) SK-MEL-30-control, and (d) PAT-73-control. Findings show consistent overlays across our embedded space (left) for a given sample-treatment protocol, and average spectra well within the ±1 standard deviation (right).

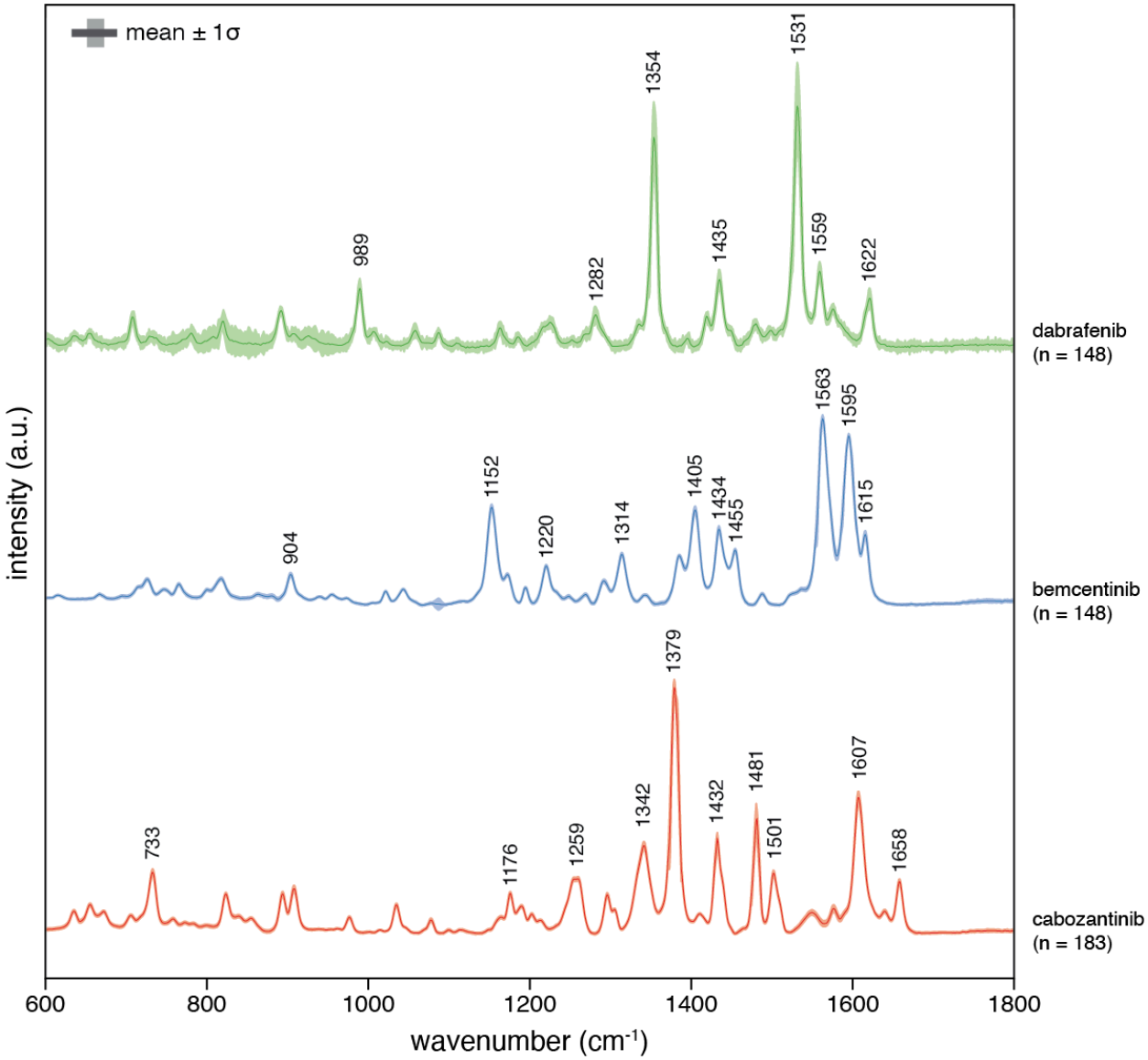

Supplementary Figure 3. Raman spectra of molecular inhibitors. Mean normalized spectra and ±1 standard deviation for targeted inhibitors cabozantinib, bemcentinib, and dabrafenib. Wavenumber assignments are annotated for each averaged spectra.

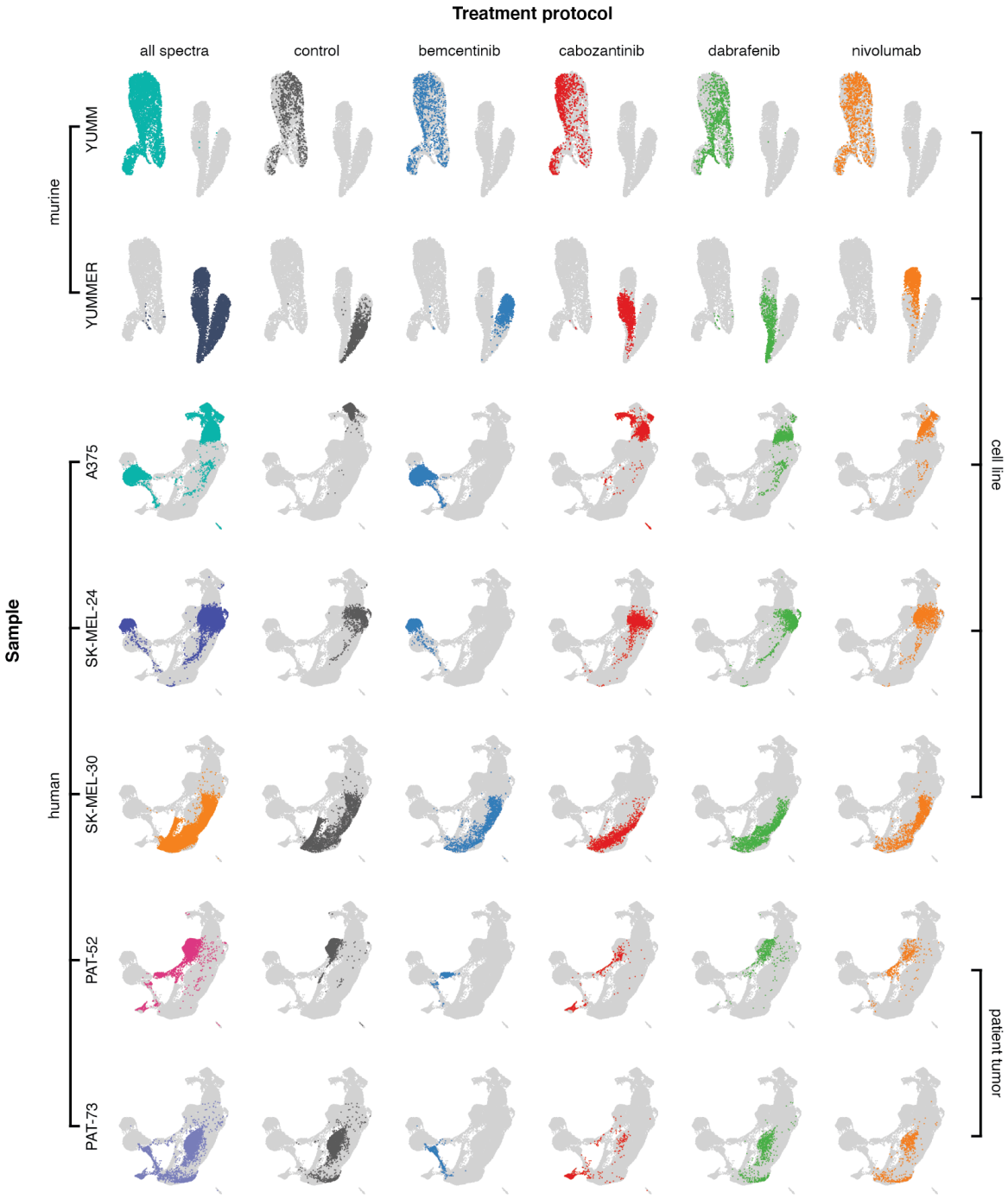

Supplementary Figure 4. One-vs-all cell spectra for mouse and human samples. Latent space localizations of mouse and human line samples discussed in Figure 3 and 4. For each sample, spectra are highlighted with respect to cell procurement source (row) and treatment protocol (column). The first column encompasses all affiliated cell spectra acquired for a given sample, and each successive column represents either an untreated cell set (control) or persistent cells measured following a treatment protocol.

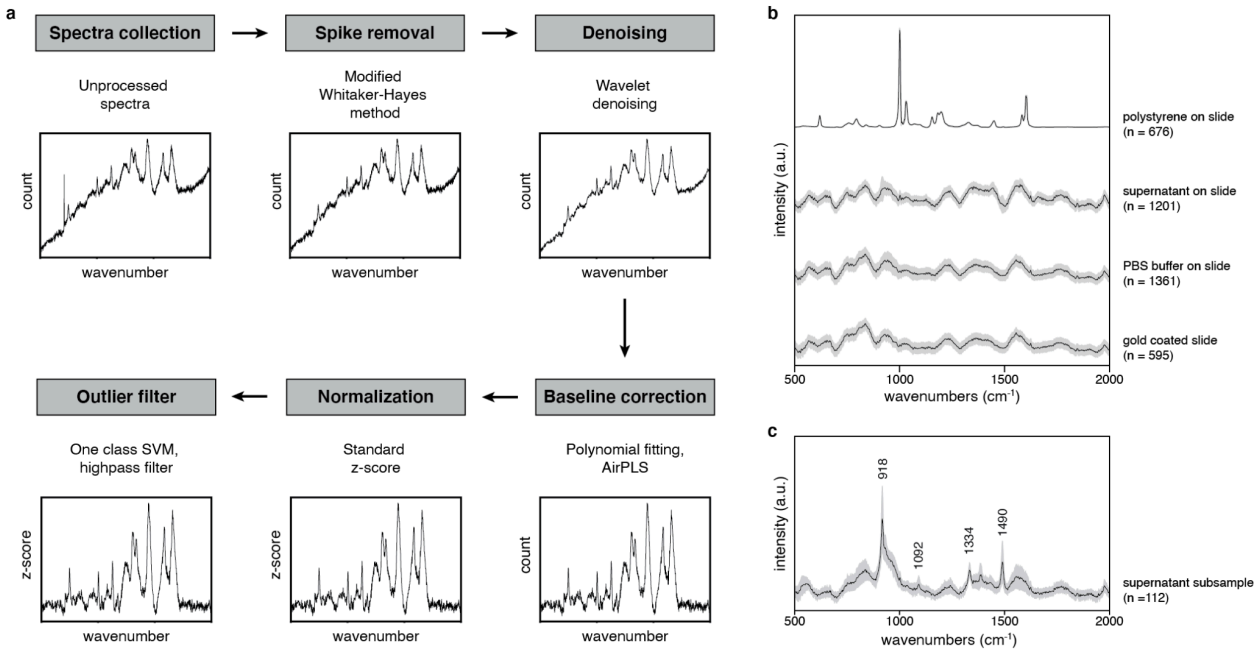

Supplementary Figure 5. Workflow of Raman spectra preprocessing. A) Representative workflow of the preprocessing steps taken for each spectrum. Preprocessing was essential to normalize and remove artifacts for cell spectra comparisons. An example spectrum of RAW264.7 is shown, highlighting the post-processed spectra after each step. B) Averaged spectra with ±1 standard deviation of post-processed background and outlier spectra acquired for our automated data filter step. The data filter step utilizes a combination of single class support vector machines (SVMs) and high-pass z-score values, and occurs after the preprocessing workflow highlighted in (A). C) A subset of spectra in the supernatant spectral set in (B) where major peak assignments are shared with polymers such as polyoxymethylene copolymer (POM-C) found in literature.

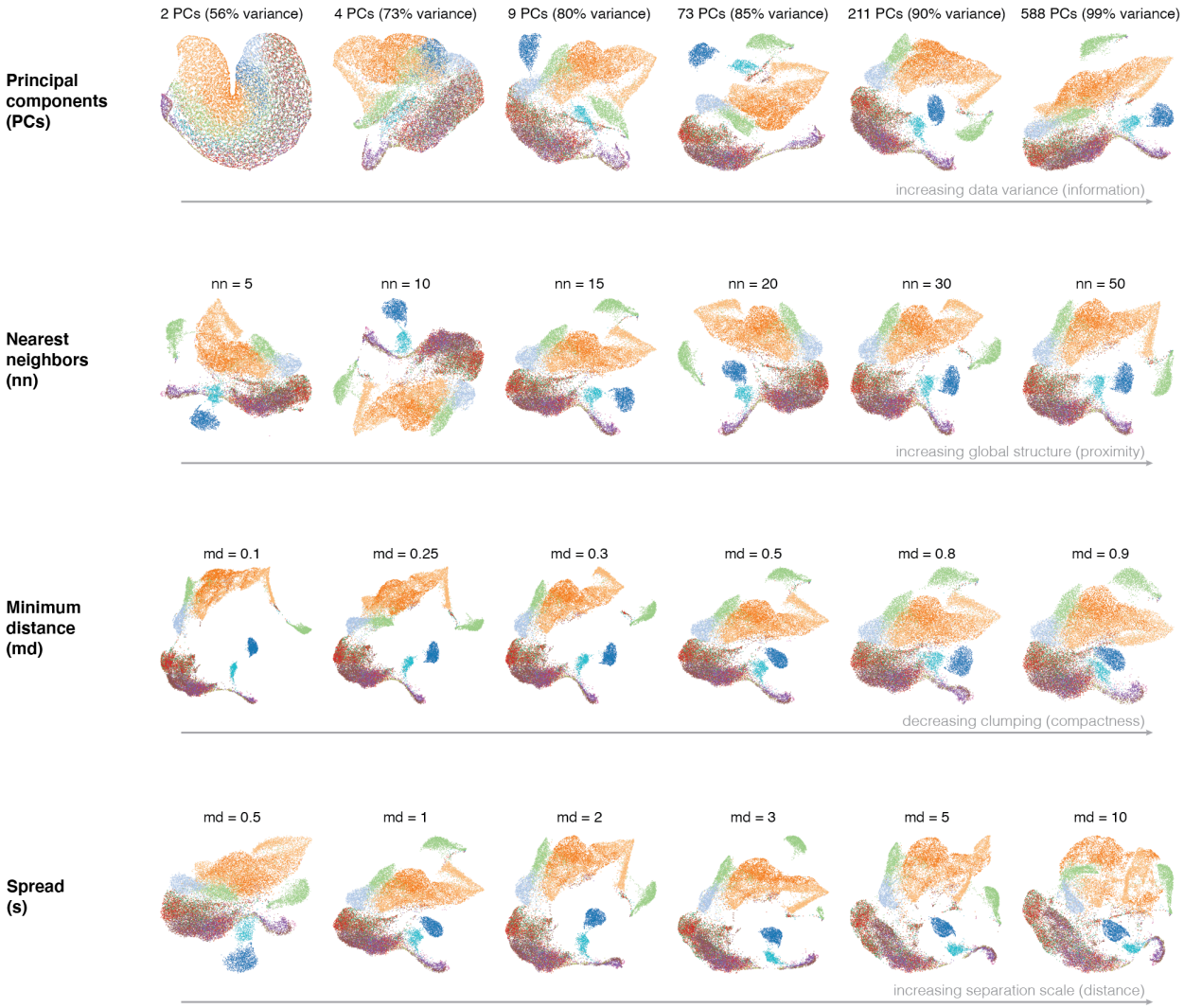

Supplementary Figure 6. Hyperparameter effects on our data clustering and analysis. Color corresponds to sample origin as defined in Figure 5 in the main text. Increasing the number of principal components retained more information and improved cell cluster separability. Increasing nearest neighbors examined more interconnectivity and preserved global structuring over local structures. Increasing minimum distance raised the lower bound of embedding space distance among points and decreased cell spectra crowding. Increasing spread enlarges the distribution of distances and affects the perceived distance between spectra.

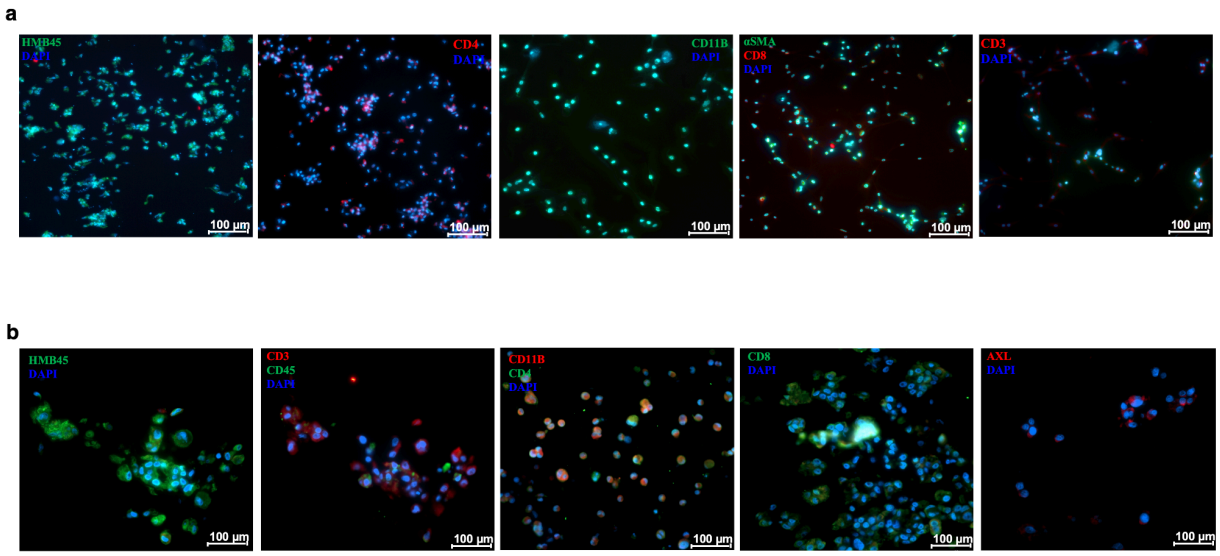

Supplemental Figure 7. Immunofluorescence of patient samples. Melanoma patient-derived samples retain immune cell composition and other cell types. A) PAT-52 patient-derived cells were allowed to grow for 7 days without passaging, and immunofluorescent tagging was applied with markers HMB-45, CD4, CD11B, α-SMA, CD8, and CD3. Scale bar, 100 µm. B) Images of PAT-73 patient-derived cells were allowed to grow for 7 days without passaging and immunofluorescent tagging was applied with markers HMB-45, CD3, CD45, CD11B, CD4, CD8, and AXL. Scale bar, 100 µm.

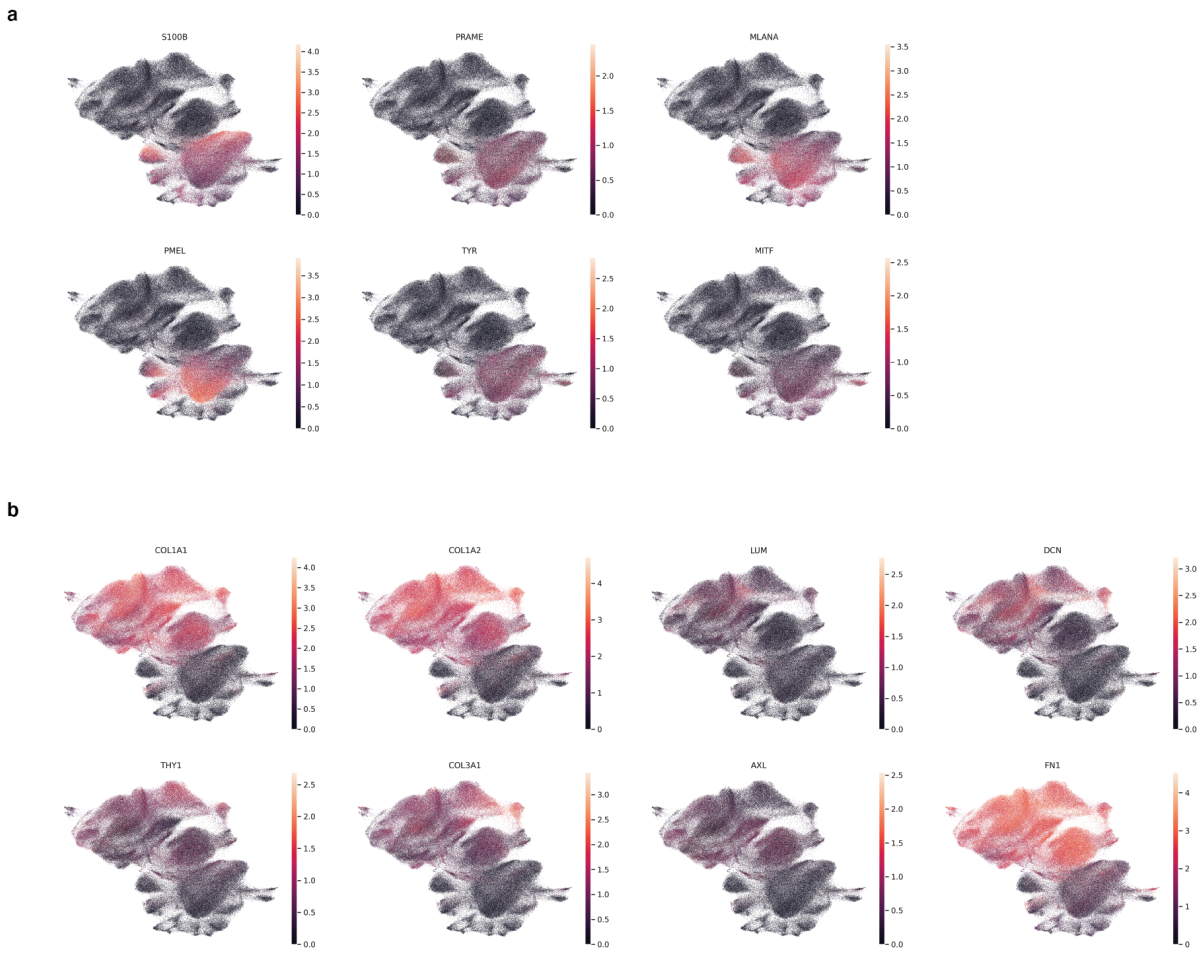

Supplementary Figure 8. Feature plots of patient melanoma samples. A) UMAP of our scRNA-seq dataset colored by marker genes S100B, PRAME, MLANA, PMEL, TYR, and MITF. The clusters with higher expressions of such genes are suggestive of tumor cells. B) UMAP of our scRNA-sequenced dataset colored by marker genes COL1A1, COL1A2, LUM, DCN, THY1, COL3A1, AXL, and PN1. The clusters with higher expressions of such genes are suggestive of fibroblast-like cells.

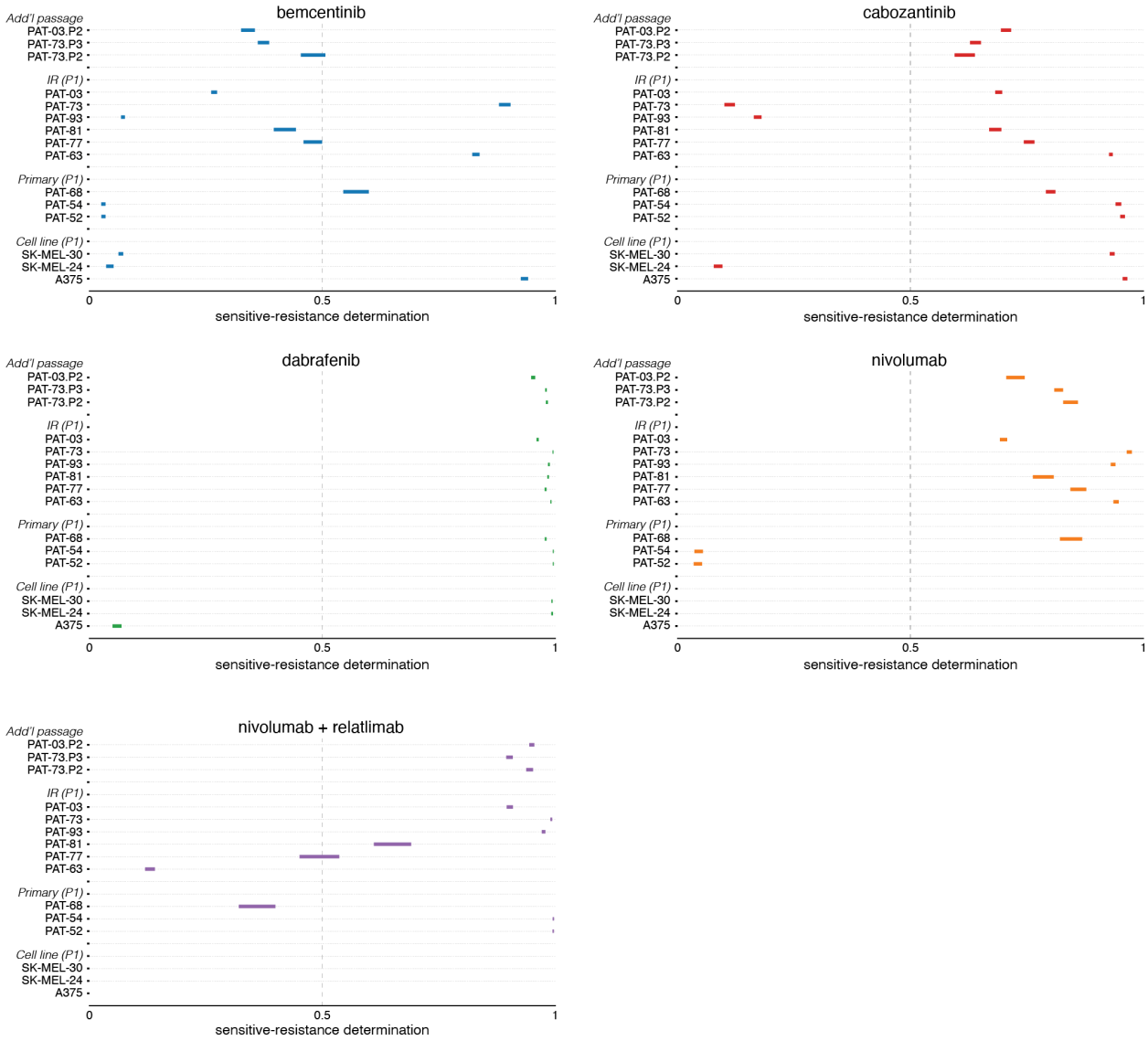

Supplementary Figure 9. Percentile distribution of mini patient responses. Response determination distribution for all mini patients sampled in each patient-derived cell line (seen and unseen by our ML model) across targeted and immunotherapy regimes. Bars represents the 5th to 95th percentile of the mini patient response.

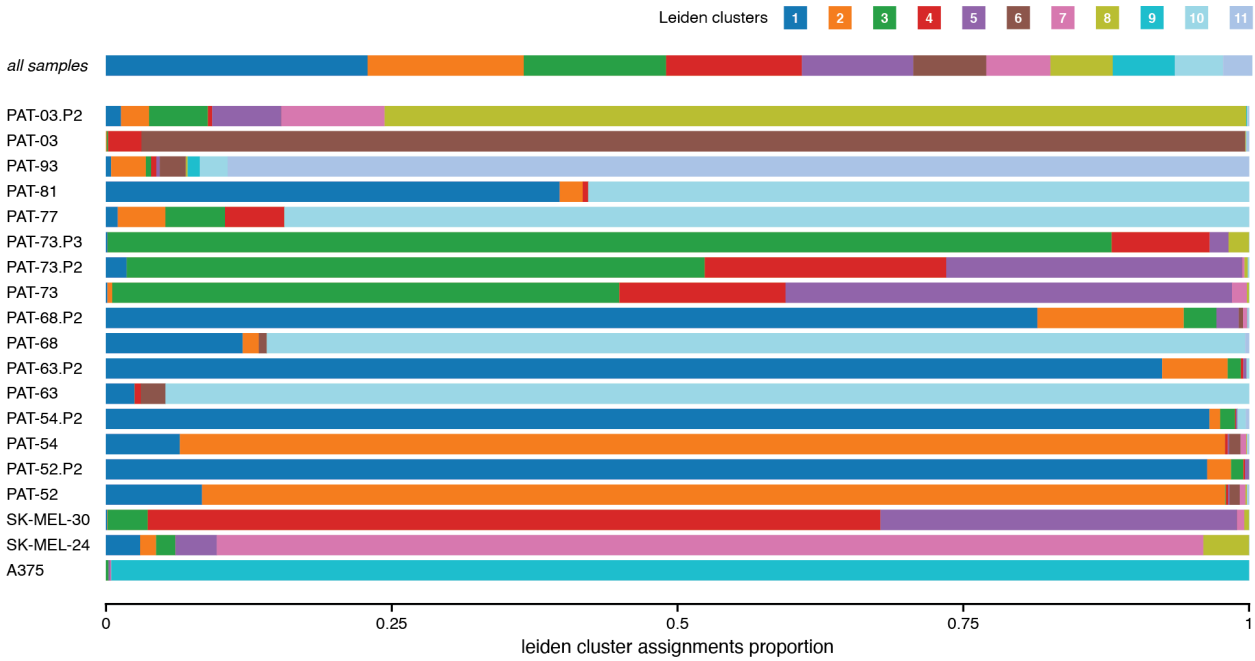

Supplementary Figure 10. Leiden cluster designation for patient-derived samples. Leiden cluster assignment proportions across each sample utilized in our patient prediction workflow, as well as the leiden cluster distribution encompassing our global dataset.

Supplementary Tables

Mouse cell line viability				
Cell line	**Bem**	**Cabo**	**Dabra**	**Nivo**
YUMM1.7	68.3	74.4	77.0	71.4
YUMMER1.7	57.1	82.8	89.2	81.1

Human cell line viability				
Cell line	**Bem**	**Cabo**	**Dabra**	**Nivo**
A375	86.1	76.1	66.1	82.7
SK-MEL-24	61.3	64.7	84.6	78.6
SK-MEL-30	70.5	79.8	78.6	80.1

Patient derived tumor line cell viability						
Sample ID	**Bem**	**Cabo**	**Dabra**	**Nivo**	**Nivo + Rela**	**Clinical**
PAT-52	62.9	82.6	91.6	40.5	80.4	-
PAT-54	70.4	72.4	89.6	45.6	85.4	-
PAT-63	74.1	80.4	82.4	78.6	24.6	NR (Nivo); R (Nivo + Rela)
PAT-73	92.0	71.2	92.1	86.7	90.6	NR (Nivo)
PAT-93	52.4	69.4	82.4	66.1	90.4	NR (Dabra); NR (Nivo)
PAT-68	83.4	85.2	74.8	86.4	27.4	NR (Nivo)
PAT-03	62.7	65.4	81.9	66.1	-	-
PAT-81	90.1	78.4	81.9	91.7	92.7	NR (Dabra); NR (Nivo)
PAT-77	86.4	76.4	74.0	82.9	86.6	NR (Nivo); NR (Nivo + Rela)
PAT-03.P2	72.7	73.4	80.4	70.1	-	-
PAT-73.P2	89.0	61.2	81.1	85.7	89.0	-
PAT-73.P3	71.0	77.2	89.1	90.7	91.1	-

Supplementary Figure 1. Cell viability data of mice and human melanoma samples. In vitro cell viability assessments for the first passages were determined after 24 hour incubation of inhibitors with concentrations described in Table 3 to observe cell response for mice samples and human samples. Additionally, cell viability was determined for later passages on select patients of interest (PAT-73, PAT-03). Viability values correspond to relative percentage to untreated control samples. For the patient resistance determination model, resistant or sensitive labels were assigned based on cell viability inference or clinical outcomes in select cases. No clinical outcome labels (R for responder and NR for nonresponder) conflicted with cell viability observations.

Inhibitor concentrations (μM)					
Sample	**Bem**	**Cabo**	**Dabra**	**Nivo**	**Nivo + Rela**
YUMM1.7	1	7	1	5	-
YUMMER1.7	1	8.5	3.5	8	-
A375	8	7.5	5	5	-
SK-MEL-24	8	9.5	10	10	-
SK-MEL-30	8.5	8.5	1	8	-
Patient derived tumor lines	8	9.5	5	6	6 + 7

Supplementary Table 2. Inhibitor concentrations used in each of our datasets.

Cell response cell count					
Cell line	Control	Bem	Cabo	Dabra	Nivo
YUMM1.7	886	1025	1146	1081	1004
YUMMER1.7	1078	961	958	838	960
A375	1291	3103	2884	1267	1303
SK-MEL-24	1299	1473	1423	1422	1430
SK-MEL-30	3327	1506	1366	1680	1380
PAT-52	1584	430	336	505	455
PAT-73	2131	406	566	761	593

Patient control cell count	
Sample ID	Count
PAT-52	1581
PAT-54	1609
PAT-63	557
PAT-68	284
PAT-73	2131
PAT-77	96
PAT-81	199
PAT-93	657
PAT-03	1512
PAT-03.P2	1591
PAT-73.P2	985
PAT-73.P3	1388

Patient control cell count	
Sample ID	Count
PAT-52.P2	1391
PAT-54.P2	1386
PAT-68.P2	1381
PAT-63.P2	1329

Supplementary Table 3. Spectra count acquired for each sample utilized in our response or determination dataset. The first table represents spectra counts utilized in observing cell response to inhibitor presence. The second table represents spectra counts utilized in our patient prediction model analysis. The third table represents spectra counts from additional passages of select patients used in understanding passage shift.

Supplementary Table 4. Raman band assignments associated with tumor immune microenvironment cells.

Raman band (cm^{-1})	Band assignment	Biological group	Reference
644-645	C-C twisting in Tyrosine	Proteins	1–4
654	Tyrosine, G	Proteins, Nucleic acid	5
667	T, G	Nucleic acids	2,6
708	C	Nucleic acids	7,8
731	A (ring breathing)	Nucleic acids	2
745-750	Ring breathing vibrations of nucleic acids Tryptophan	Nucleic acids Proteins	9
779-784	C, U (ring breathing), PO2- backbone stretch	Nucleic acids	2,10
805	PO2- symmetric stretch	Nucleic acids	11
826	Tyrosine (ring breathing)	Proteins	12
833-836	PO2- symmetric stretch	Nucleic acids	12
841-843	Polysaccharide, Glucose	Carbohydrates	6
851	C-C stretch in Tyrosine and Valine	Proteins	13
883	CH2 rocking	Proteins	6
888	Tyrosine	Proteins	14
904	Tyrosine Glycogen	Proteins Carbohydrates	15,16
912	Glucose	Carbohydrates	6,17
917	C-C stretch	Proteins	17
924	Proline ring	Protein	11
927-930	C-C skeletal stretch	Proteins	6,12
958-959	CH3 deformations	Lipids, Proteins	18
968	Phosphatidylcholine	Lipids	12
998-1003	C-C aromatic symmetric ring breathing of phenylalanine	Proteins	19–21
1021	Glycogen	Carbohydrates	6
1030-1032	C-N in-plane bending of phenylalanine	Proteins	12
1080-1082	C-C	Lipids	22,23

	PO2 symmetric stretch	Nucleic acids	
1126-1129	C–C stretch C–N stretch	Lipids Proteins	1,21
1156-1158	C-C stretch, C-N stretch	Beta-carotene Proteins	4,23–25
1173-1174	Tyrosine, Phenylalanine	Proteins	2
1207	C-C6H5 stretch in phenylalanine and tryptophan Tyrosine	Proteins	12,26
1220	Amide III	Proteins	27
1225	Amide III	Proteins	6
1241	T, Amide III	Nucleic acids Proteins	2
1250-1252	Amide III	Proteins	12
1274	Amide III	Proteins	28
1303-1306	A (ring mode), C-H deformation CH2 twist	Nucleic acids Proteins Lipids	2,12,29,30
1308-1310	CH2 deformation, CH3CH2 twisting	Lipids	9,26
1312	CH3CH2 twisting	Proteins, Lipids	27
1336	CH3, CH2 wagging, C-H deformation, C-C stretch	Proteins, Lipids, Carbohydrates	13,31
1337	A, G (ring mode)	Nucleic acids	25
1352	G Tryptophan	Nucleic acids Proteins	32
1361	Tryptophan	Proteins	17
1382	CH3 symmetric deformation Ring breathing modes of the nucleic acids	Lipids Nucleic acids	33
1385	C-C linear stretch CH3 symmetric deformation	Melanin Lipids	34–37
1400	U, A	Nucleic acids	8
1410-1413	CH deformation	Proteins Lipids	38
1419-1420	CH2 scissoring A, G	Lipids Nucleic acids	12
1433-1440	CH2 deformation, C=C stretch unsaturated fatty acids	Lipids	9,10

1445-1447	CH2 bend CH2 deformation	Proteins Lipids	2,10,21
1457-1460	CH2 deformation, CH deformation	Proteins	2,12
1470	G, A	Nucleic acid	39
1482	G, A (ring mode)	Nucleic acids	12
1497	C-NH2 scissoring	Nucleic acids	40
1518	C=C stretch	Carotenoid	6
1526-1527	C=C	Carotenoids	2
1553	Tryptophan	Proteins	12
1562	C-N and N-H vibrations Tryptophan A, G ring breathing	Proteins Nucleic acids	33
1575	C-C ring stretch	Nucleic acids	12,13
1580	Aromatic ring in-plane stretch	Melanin	34
1582-1588	A,G C=C olefinic stretch	Nucleic acids Proteins	6,9,23,34–36, 41
1591-1593	C=C in-plane bending mode in Phenylalanine	Proteins	37
1606	C=C stretch in Phenylalanine	Proteins	42
1610	aromatic ring stretch in Tyrosine	Proteins	4
1624	C=C bend in tryptophan	Proteins	40
1636	Amide I	Proteins	6
1652-1658	C=C stretch, Amide I	Lipids, Proteins	9,25,37
1660-1666	Amide I	Proteins	12,26
1672	Amide I	Proteins	13,28
1681-1684	U (C=O stretch)	Nucleic acids	12
1692	Amide I	Proteins	7
1736-1775	C=O stretch	Lipids	23,37,43
1791-1797		Unassigned	44

1. Chaudhary, N., Nguyen, T. N. Q., Cullen, D., Meade, A. D. & Wynne, C. Discrimination of immune cell activation using Raman micro-spectroscopy in an in-vitro & ex-vivo model. *Spectrochim Acta A Mol Biomol Spectrosc* **248**, 119118 (2021).
2. Brauchle, E. *et al.* Raman spectroscopy as an analytical tool for melanoma research. *Clin Exp Dermatol* **39**, 636–645 (2014).
3. Qiu, X. *et al.* Raman spectroscopy combined with deep learning for rapid detection of melanoma at the single cell level. *Spectrochim Acta A Mol Biomol Spectrosc* **286**, 122029 (2023).
4. Xie, Y., Zhang, D., Jarori, G. K., Davisson, V. J. & Ben-Amotz, D. The Raman detection of peptide tyrosine phosphorylation. *Anal Biochem* **332**, 116–121 (2004).
5. Zhang, P. *et al.* Label-Free Exosomal Detection and Classification in Rapid Discriminating Different Cancer Types Based on Specific Raman Phenotypes and Multivariate Statistical Analysis. *Molecules* **24**, (2019).
6. Movasaghi, Z., Rehman, S. & Rehman, I. U. Raman Spectroscopy of Biological Tissues. *Applied Spectroscopy Reviews* **42**, 493–541 (2007).
7. Wang, J. *et al.* Raman spectroscopic study of cervical precancerous lesions and cervical cancer. *Lasers Med Sci* **36**, 1855–1864 (2021).
8. Bankapur, A., Zachariah, E., Chidangil, S., Valiathan, M. & Mathur, D. Raman tweezers spectroscopy of live, single red and white blood cells. *PLoS One* **5**, e10427 (2010).
9. Feuerer, N. *et al.* Lipidome profiling with Raman microspectroscopy identifies macrophage response to surface topographies of implant materials. *Proceedings of the National Academy of Sciences* **118**, e2113694118 (2021).
10. Naumann, M. *et al.* Label-Free Characterization of Macrophage Polarization Using Raman Spectroscopy. *International Journal of Molecular Sciences* **24**, 824 (2023).
11. Mahadevan-Jansen, A. & Richards-Kortum, R. R. Raman spectroscopy for the detection of cancers and precancers. *J Biomed Opt* **1**, 31–70 (1996).
12. Terentis, A. C., Fox, S. A., Friedman, S. J. & Spencer, E. S. Confocal Raman microspectroscopy discriminates live human metastatic melanoma and skin fibroblast cells. *Journal of Raman*

Spectroscopy **44**, 1205–1216 (2013).

13. Zhou, Q.-Q. *et al.* Rapid visualization of PD-L1 expression level in glioblastoma immune microenvironment via machine learning cascade-based Raman histopathology. *J Adv Res* **65**, 257–271 (2024).
14. Chen, X., Li, X., Yang, H., Xie, J. & Liu, A. Diagnosis and staging of diffuse large B-cell lymphoma using label-free surface-enhanced Raman spectroscopy. *Spectrochim Acta A Mol Biomol Spectrosc* **267**, 120571 (2022).
15. Lee, S. *et al.* Early-stage diagnosis of bladder cancer using surface-enhanced Raman spectroscopy combined with machine learning algorithms in a rat model. *Biosens Bioelectron* **246**, 115915 (2024).
16. Mert, S., Özbek, E., Ötünçtemur, A. & Çulha, M. Kidney tumor staging using surface-enhanced Raman scattering. *J Biomed Opt* **20**, 047002 (2015).
17. Chang, M. *et al.* RaT: Raman Transformer for highly accurate melanoma detection with critical features visualization. *Spectrochimica Acta Part A: Molecular and Biomolecular Spectroscopy* **305**, 123475 (2024).
18. Nijssen, A. *et al.* Discriminating basal cell carcinoma from its surrounding tissue by Raman spectroscopy. *J Invest Dermatol* **119**, 64–69 (2002).
19. You, C., Yi, J.-Y., Hsu, T.-W. & Huang, S.-L. Integration of cellular-resolution optical coherence tomography and Raman spectroscopy for discrimination of skin cancer cells with machine learning. *JBO* **28**, 096005 (2023).
20. Ribeiro, A. R. B. *et al.* Application of Raman spectroscopy for characterization of the functional polarization of macrophages into M1 and M2 cells. *Spectrochim Acta A Mol Biomol Spectrosc* **265**, 120328 (2022).
21. Wen, J. *et al.* Detection and Classification of Multi-Type Cells by Using Confocal Raman Spectroscopy. *Front. Chem.* **9**, 641670 (2021).
22. Yang, C. *et al.* The Identification of Breast Cancer Subtypes by Raman Spectroscopy Integrated With Machine Learning Algorithms: Analyzing the Influence of Baseline. *Journal of Raman Spectroscopy* (2025) doi:10.1002/jrs.6799.
23. Rimskaya, E. *et al.* Multi-Wavelength Raman Differentiation of Malignant Skin Neoplasms.

International Journal of Molecular Sciences **25**, 7422 (2024).

24. Huang, L. *et al.* Rapid, label-free histopathological diagnosis of liver cancer based on Raman spectroscopy and deep learning. *Nature Communications* **14**, 1–14 (2023).
25. Feng, X. *et al.* Raman active components of skin cancer. *Biomed Opt Express* **8**, 2835–2850 (2017).
26. Xie, J., Wei, Y., Liang, X., Ma, C. & Su, X. In situ single-cell spontaneous Raman spectroscopy differentiates tumor-associated macrophages. *Sensors and Actuators B: Chemical* **417**, 136053 (2024).
27. Lazaro-Pacheco, D., Shaaban, A. M., Rehman, S. & Rehman, I. Raman spectroscopy of breast cancer. *Applied Spectroscopy Reviews* (2020) doi:10.1080/05704928.2019.1601105.
28. Gniadecka, M. *et al.* Melanoma diagnosis by Raman spectroscopy and neural networks: structure alterations in proteins and lipids in intact cancer tissue. *J Invest Dermatol* **122**, 443–449 (2004).
29. Puppels, G. J., Garritsen, H. S., Segers-Nolten, G. M., de Mul, F. F. & Greve, J. Raman microspectroscopic approach to the study of human granulocytes. *Biophys J* **60**, 1046–1056 (1991).
30. Zhang, X. *et al.* Investigation on the Cancer Invasion and Metastasis of Skin Squamous Cell Carcinoma by Raman Spectroscopy. *Molecules* **24**, 2059 (2019).
31. Danciu, C. *et al.* A characterization of four B16 murine melanoma cell sublines molecular fingerprint and proliferation behavior. *Cancer Cell Int* **13**, 75 (2013).
32. Aguilar-Hernández, I. *et al.* Discrimination of radiosensitive and radioresistant murine lymphoma cells by Raman spectroscopy and SERS. *Biomed Opt Express* **11**, 388–405 (2020).
33. Silveira, L., Jr, Silveira, F. L., Bodanese, B., Zângaro, R. A. & Pacheco, M. T. T. Discriminating model for diagnosis of basal cell carcinoma and melanoma in vitro based on the Raman spectra of selected biochemicals. *J Biomed Opt* **17**, 077003 (2012).
34. Huang, Z. *et al.* Raman spectroscopy of in vivo cutaneous melanin. *JBO* **9**, 1198–1205 (2004).
35. Yakimov, B. P. *et al.* Melanin distribution from the dermal–epidermal junction to the stratum corneum: non-invasive in vivo assessment by fluorescence and Raman microspectroscopy. *Scientific Reports* **10**, 1–13 (2020).
36. Lim, L. *et al.* Clinical study of noninvasive in vivo melanoma and nonmelanoma skin cancers using multimodal spectral diagnosis. *J Biomed Opt* **19**, 117003 (2014).

37. Paidi, S. K. *et al.* Raman Spectroscopy and Machine Learning Reveals Early Tumor Microenvironmental Changes Induced by Immunotherapy. *Cancer Res* **81**, 5745–5755 (2021).
38. Kourkoumelis, N. *et al.* Advances in the in Vivo Raman Spectroscopy of Malignant Skin Tumors Using Portable Instrumentation. *Int J Mol Sci* **16**, 14554–14570 (2015).
39. Short, K. W., Carpenter, S., Freyer, J. P. & Mourant, J. R. Raman spectroscopy detects biochemical changes due to proliferation in mammalian cell cultures. *Biophys J* **88**, 4274–4288 (2005).
40. Pezzotti, G. Raman spectroscopy in cell biology and microbiology. *Journal of Raman Spectroscopy* **52**, 2348–2443 (2021).
41. Borek-Dorosz, A. *et al.* Raman-based spectrophenotyping of the most important cells of the immune system. *J Adv Res* **41**, 191–203 (2022).
42. Sigle, M. *et al.* Translating genomic tools to Raman spectroscopy analysis enables high-dimensional tissue characterization on molecular resolution. *Nature Communications* **14**, 1–16 (2023).
43. Elumalai, S., Managó, S. & De Luca, A. C. Raman Microscopy: Progress in Research on Cancer Cell Sensing. *Sensors* **20**, 5525 (2020).
44. Grajales Lopera, D. O. *et al.* Image-guided Raman spectroscopy navigation system to improve transperineal prostate cancer detection. Part 2: in-vivo tumor-targeting using a classification model combining spectral and MRI-radiomics features. *J Biomed Opt* **27**, (2022).